Autolamellasomes: An Autophagy-Dependent Parallel Pathway for Bulk ER Degradation and Lysosome Biogenesis

Di Lu[1*], Rouxuan Zhang[2], Wanjing Shi[1], Delin Zhan[1], Yuntian Yang[1], Xulin Sun[1], Han Zhang[1], Ying Li[3], Xueming Li[2] and Li Yu[1*]

[1]The State Key Laboratory of Membrane Biology, Tsinghua University-Peking University Joint Center for Life Sciences, Beijing Frontier Research Center for Biological Structure, School of Life Sciences, Tsinghua University, Beijing 100084, China.

[2] The State Key Laboratory of Membrane Biology, Tsinghua University-Peking University Joint Center for Life Sciences, Beijing Frontier Research Center for Biological Structure, MOE Key Laboratory of Protein Sciences, School of Life Sciences, Tsinghua University, Beijing 100084, China.

[3]Technology Center for Protein Sciences, School of Life Sciences, Tsinghua University, Beijing, China.

* Correspondence: Li Yu, liyulab@mail.tsinghua.edu.cn;

Di Lu, ld2023@mail.tsinghua.edu.cn

Abstract

Autophagy maintains cellular homeostasis through lysosomal degradation of cytoplasmic components, yet how prolonged autophagy activation reshapes organelle architecture remains poorly understood. Here we identify a previously unrecognized form of endoplasmic reticulum (ER) remodeling induced by chronic mTOR inhibition. We show that sustained autophagy triggers the formation of multilamellar ER-derived structures, termed autolamellasomes, which mediate bulk ER degradation. Unlike canonical ER-phagy, autolamellosome biogenesis requires the core autophagy machinery but is independent of all known ER-phagy receptors. Using cryo-electron tomography, correlative light–electron microscopy, and *in vitro* reconstitution, we

demonstrate that autolamellasomes arise through autophagy-dependent assembly and compaction of fragmented ER membranes into concentric stacks subsequently engulfed by lysosomes. Autolamellosomes form constitutively at low levels across diverse cell types, accumulate in senescent cells and fibroblasts from Hutchinson–Gilford progeria syndrome (HGPS), and thus represent an aging-associated pathway linking sustained mTOR suppression to ER and lysosomal homeostasis. This work not only resolves the long-standing origin of intra-lysosomal membrane whorls but also establishes a cell-free system for dissecting autophagy-driven membrane remodeling, revealing a conserved degradative route coupling nutrient sensing to membrane turnover, lipid catabolism, and aging.

Key words

Autolamellasome, Autophagy, ER, Lysosome, mTOR

Introduction

Autophagy is an evolutionarily conserved catabolic process essential for maintaining cellular homeostasis in eukaryotes[1-4]. This lysosomal degradation pathway ensures the continuous turnover of cytoplasmic components—ranging from proteins and lipids to entire organelles—thereby supplying nutrients during starvation and removing damaged or superfluous structures[5-7]. The best-characterized form, macroautophagy (hereafter referred to as autophagy), entails the de novo formation of a double-membrane vesicle known as the autophagosome, which engulfs cytoplasmic cargo and delivers it to lysosomes for degradation[8-10].

Originally regarded as a non-selective “bulk” degradation process activated by nutrient deprivation, autophagy is now recognized as a highly selective and precisely regulated system[11-14]. Distinct selective autophagy pathways—including ER-phagy, mitophagy, xenophagy, and aggrephagy—target specific substrates such as damaged mitochondria,

intracellular pathogens, or protein aggregates[15]. This selectivity is conferred by cargo receptors containing LC3-interacting region (LIR) motifs that bridge designated cargo to the Atg8/LC3 family proteins decorating the phagophore[16-19].

A paradigmatic example of such precision is endoplasmic reticulum autophagy (ER-phagy), a process that controls ER size, morphology, and function through the lysosomal turnover of ER subdomains[20]. The ER forms a dynamic network responsible for protein synthesis, lipid metabolism, and calcium storage; its homeostasis is critical for cell survival and stress adaptation[21,22]. ER-phagy can occur via several morphologically distinct routes: (1) macro-ER-phagy, in which ER fragments are sequestered by autophagosomes[23]; (2) micro-ER-phagy, involving direct lysosomal invagination and engulfment of ER regions[24]; (3) ER-to-lysosome–associated degradation (ERLAD), where ER-derived vesicles directly fuse with endolysosomes; and most importantly, receptor-mediated ER-phagy[25,26].

The initiation and specificity of receptor-mediated ER-phagy are governed by a family of ER-phagy receptors—transmembrane or membrane-associated proteins that recognize ER subdomains and recruit the autophagy machinery through conserved LIR motifs[27]. Beyond serving as tethers, many receptors such as FAM134B[28] and RTN3L[29] actively remodel the ER membrane through reticulon homology domains (RHDs) that induce curvature and fragmentation, while intrinsically disordered regions (IDRs) provide flexible linkers between ribosome-studded ER and the growing phagophore[30-32]. Distinct receptors thus confer subdomain selectivity: FAM134B preferentially targets ER sheets, whereas RTN3L and ATL3[33] act on tubules. Others, such as CCPG1, also recruit upstream autophagy regulators (e.g., FIP200), directly initiating local autophagosome formation at the ER surface[34,35]. Together, these mechanisms ensure the spatial and temporal precision of receptor-mediated ER turnover.

A morphological hallmark of lysosomes is their dense, lamellar content composed of

intraluminal vesicles and membrane whorls[36]. Under various physiological or pathological conditions, lamellated membrane structures—including membrane whorls[37], myelin figures, and zebra bodies[38]—have long been observed within lysosomes in diverse contexts such as autophagy, drug-induced phospholipidosis[39], and lysosomal storage disorders like Fabry disease[38,40,41]. These concentric, multilamellar stacks are thought to arise when membrane-rich autophagic cargo resists lysosomal degradation, leading to lipid reorganization into multilamellar arrays[42]. Pharmacological or genetic disruption of lipid catabolism similarly promotes such lamellation. First described by Rozenszajn et al. in 1969[43], these structures remain a morphological hallmark of lysosomes, and their increased abundance is a sign of lysosomal dysfunction. However, the biophysical mechanisms underlying their initiation and persistence remain elusive.

In yeast, ER stress triggers the formation of large multilamellar ER whorls that are eliminated via a micro-ER-phagy route distinct from canonical autophagy[24]. This process involves direct invagination of the vacuolar membrane, depends on the ESCRT machinery[44] and the ER-localized Nem1-Spo7 phosphatase complex, but proceeds independently of ATG genes and classical ER-phagy receptors[45]. In mammalian cells, severe ER stress similarly induces the formation of massive, concentric ER whorls—up to 10 μm in diameter—through a PERK- and COPII-dependent pathway. These structures function to alleviate ER stress by concentrating PERK and sequestering translocons[46], and their formation and clearance are likewise independent of macro- and micro-autophagy.

Here, we identify a distinct form of ER remodeling that emerges under chronic mTOR inhibition—a condition that persistently activates autophagy[47]. We show that prolonged mTOR suppression triggers the formation of extensive multilamellar ER-derived structures, which we term autolamellasomes. Unlike conventional double-membrane autophagosomes, autolamellasomes are composed of densely packed, concentric ER

membranes that are subsequently engulfed by lysosomes for degradation. Genetic and biochemical analyses reveal that their formation requires the core autophagy machinery but proceeds independently of all known ER-phagy receptors, defining a unique, autophagy-dependent yet receptor-independent ER remodeling and degradation pathway. Using cell-free reconstitution, we demonstrate that autolamellasomes arise from the autophagy-driven assembly and compaction of fragmented ER membranes. They are detectable under basal conditions but markedly accumulate in senescent cells and in fibroblasts derived from Hutchinson–Gilford progeria syndrome (HGPS) patients, consistent with chronic mTOR inhibition during aging. Temporally, autolamellosome formation follows conventional autophagosome-mediated cytosolic degradation and facilitates the bulk catabolism of lipid-rich ER membranes, sustaining long-term energy balance under nutrient stress.

Together, these findings define autolamellasomes as a parallel structure to autophagosomes that mediates bulk ER degradation under prolonged mTOR inhibition, linking mTOR signaling to membrane homeostasis and cellular aging.

Results

Prolonged mTOR Inhibition Induces the Formation of "Free Whorls"

Prolonged inhibition of mTOR by Torin1 led to the accumulation of numerous whorl-like membrane structures within autolysosomes (Fig. 1A). It is well-established that mTOR inhibition induces autophagy, characterized by the transient appearance of double-membraned autophagosomes. However, transmission electron microscopy (TEM) analysis revealed that 24 hours after Torin1 treatment, typical autophagosomes were rarely observed. Instead, cells contained abundant autolysosomes filled with densely packed membrane whorls with size of ~ 500 nm-2 μm, Intriguingly, we also observed multilamellar whorls composed of stacked double membranes that were not enclosed by a limiting membrane with similar size with whorls inside autolysosome. Because these structures resided outside autolysosomes, we refer to them as "free

whorls" (Fig. 1B).

Free whorls were frequently observed in close proximity to the endoplasmic reticulum (ER). Notably, at the time points when free whorls appeared, conventional double-membraned autophagosomes were nearly undetectable. Time-course TEM analysis revealed that free whorls began to emerge approximately 4 hours after starvation and progressively accumulated with prolonged treatment (Fig.1C). The number of autolysosomes or lysosomes containing whorls increased with a similar trajectory (Fig.1C), and the number of internal whorls within each whorl-bearing lysosome rose correspondingly (Fig.1D). Similarly, inhibition of mTOR by other means—including rapamycin treatment and nutrient deprivation—also induced prominent whorl formation (Fig.2Q-2R). Moreover, this phenomenon was consistently observed across all tested cell lines derived from multiple species, although the abundance of free whorls and whorl-containing lysosomes varied among different cell types (Fig.1H, Extended Fig.1A-1B).

Because chemical fixation can potentially introduce artifacts, we next employed cryo-electron tomography (cryo-ET), which preserves native membrane ultrastructure with high fidelity. Cryo-ET unambiguously confirmed the presence of free whorls and revealed that each consisted of multiple concentric double membranes with a luminal spacing of ~15 nm (Fig.1E-1F). Three-dimensional FIB-SEM further demonstrated that each whorl forms a spherical structure (Fig.1G).

Together, these findings indicate that prolonged mTOR inhibition triggers the formation of multilamellar free whorls, which subsequently appear to be engulfed by autolysosomes or lysosomes, revealing an unexpected ultrastructural consequence of sustained mTOR suppression.

The Free Whorls Originate from the Endoplasmic Reticulum

The frequent association of free whorls with the endoplasmic reticulum (ER) suggested that they may arise from the ER. To test this hypothesis, we first labeled live cells with ER-Tracker and observed that prolonged mTOR inhibition transformed the ER morphology from a reticular network into punctate structures (Fig.2A). Co-labeling with LAMP1-YFP and mCherry-REEP5 revealed the appearance of LAMP1-YFP^{-}/mCherry-REEP5^{+} puncta, as well as the translocation of mCherry-REEP5 signal into LAMP1-YFP^{+} lysosomes or autolysosomes (Fig.2C). Three-dimensional confocal imaging confirmed the existence of these REEP5-positive puncta (Fig.2D).

To exclude potential artifacts caused by the large fluorescent tag, we generated EGFP- or Halo-tagged REEP5 constructs and observed comparable puncta formation, confirming that the phenomenon is tag-independent (Extended Fig.2A, 2C). Quantitative analysis showed that nearly all cells undergoing prolonged mTOR inhibition developed ER puncta (Fig.2B, 2E-2F, Extended Fig.2B, 2D-2E). When other ER markers (mCherry-SEC61B, Calnexin-Halo, and ER-DsRed) were used, the proportion of cells with puncta was similar to that observed with REEP5 (Extended Fig.2F-2H).

To rule out artifacts arising from overexpression, we next examined endogenous ER proteins by immunostaining with antibodies against LAMP1 and either SEC61B or REEP5. Consistently, SEC61B- and REEP5-positive puncta were detected both inside and outside autolysosomes/lysosomes, supporting the conclusion that these structures are not overexpression artifacts (Fig.2G). Notably, the frequency and Pearson correlation coefficients in immunostained samples were lower than in overexpression systems, implying that ER protein overexpression can enhance puncta formation to some extent (Fig.2H-2K).

We next examined the ultrastructure of these puncta using APEX labeling for electron

microscopy. Because APEX2-catalyzed reactions generate electron-dense DAB precipitates, this method enables precise localization of tagged proteins[48]. APEX2-tagged SEC61B and REEP5 both exhibited dark, electron-dense labeling on the whorls (Fig.2L, Extended Fig.2M). Similarly, correlative light and electron microscopy (CLEM) confirmed colocalization of REEP5 signal with the whorls, providing direct evidence that the whorls originate from the ER (Fig.2M).

To capture the dynamics of ER puncta formation, we performed live-cell time-lapse imaging. The fraction of cells containing REEP5 puncta increased sharply within 5 hours after mTOR inhibition, accompanied by a parallel rise in the Pearson correlation coefficient with LAMP1-YFP (Fig.2N, Extended Fig.2I-2J). These observations indicate that ER puncta form rapidly and are subsequently delivered into autolysosomes for degradation.

Consistent with this, Western blot analysis revealed progressive degradation of ER proteins following prolonged mTOR inhibition. After 24 hours, most ER-resident proteins were degraded to varying degrees, with the notable exception of TEX264, which remained largely stable (Fig.2O). Five independent experiments confirmed this degradation pattern (Fig.2P). Label-free quantitative mass spectrometry produced similar results (Fig.2Q), although TEX264 appeared reduced in this dataset—likely reflecting normalization differences, as Western blots were normalized to actin, whereas MS data were normalized to total protein, leading to an apparent increase in actin and relative decrease in TEX264 in the Torin1-treated group.

Time-course analysis further revealed distinct degradation kinetics among ER proteins. The autophagy substrate p62 was degraded within 4 hours of mTOR inhibition, whereas ER proteins displayed diverse temporal profiles. For instance, TEX264 was degraded at early time points but its expression rebounded by 12 hours, suggesting enhanced transcription or translation. In contrast, ATL3 and REEP5 levels remained stable until

226 12 hours but declined sharply by 24 hours, while other ER proteins showed gradual
227 decreases (Fig.2R-2S).
228
229 Together, these data indicate that prolonged mTOR inhibition induces the formation of
230 ER-derived puncta, which are subsequently engulfed and degraded by
231 autolysosomes/lysosomes. The distinct kinetics and selectivity of degradation suggest
232 that multiple mechanisms—including transcriptional regulation, selective ER-phagy,
233 and puncta formation—contribute to the turnover of ER components under sustained
234 mTOR inhibition.
235
236 **Formation of Whorls Depends on the Core Autophagy Machinery but Not ER-**
237 **Phagy Receptors**
238
239 We next investigated the genetic requirements governing whorl formation. Given their
240 frequent association with ER membranes, we first examined whether known ER-phagy
241 receptors are required. Deletion of the major and widely recognized ER-phagy
242 receptors—including FAM134B[28], SEC62[49], TEX264[32,50], ATL3[33], and CCPG1[35]—did
243 not affect whorl formation. To further exclude the involvement of canonical ER-phagy
244 receptors, we generated a cell line lacking all five known receptors (FAM134B, ATL3,
245 SEC62, TEX264, and CCPG1), hereafter referred to as ERphR-KO cells. Across three
246 independently derived clones, simultaneous loss of these receptors had minimal impact
247 on whorl formation. We then asked whether genes implicated in the generation of large
248 ER whorls (~10 μm) under ER stress conditions might contribute. However, knockout
249 of these genes, or of key transcriptional regulators of the unfolded protein response
250 (UPR), similarly had no detectable effect on whorl formation (Fig.3A).
251
252 We next tested genes involved in general membrane dynamics based on functional
253 prediction. Among these, knockout of NPC2 modestly reduced whorl formation,
254 whereas deletion of PI4KIIA, VPS13C, or SCAP had no discernible effect. In striking

255 contrast, disruption of core autophagy genes markedly impaired whorl biogenesis.
256 Deletion of ATG2 (ATG2A/2B DKO), ATG7, ATG9A, or ATG8 almost completely
257 abolished whorl formation, while loss of ATG5, ATG14, ATG13, ATG16L, or ATG3
258 produced moderate reductions. Knockout of Beclin-1 or WIPI2 had a weak effect, and
259 deletion of ULK1 or p62 showed no significant impact (Fig.3A). Together, these results
260 demonstrate that the core autophagy machinery—but not canonical ER-phagy
261 receptors—is essential for whorl formation.
262
263 We next assessed how disruption of these pathways affects ER protein turnover. Two
264 complementary assays were employed. First, we monitored cleavage of mCherry-
265 REEP5, a well-established reporter for ER-phagy. Knockout of autophagy core
266 components—including ATG2, ATG5, and ATG7—completely blocked mCherry-
267 REEP5 cleavage (Fig.3B-3C). In contrast, deletion of individual ER-phagy receptors
268 (FAM134B, SEC62, ATL3) had no significant effect, while TEX264 and CCPG1
269 knockouts modestly reduced cleavage efficiency (Extended Fig.3A-3C). Second, we
270 examined endogenous ER protein degradation. Core autophagy gene deletion broadly
271 prevented degradation of multiple ER proteins, whereas ERphR-KO and individual ER-
272 phagy receptor knockout cells exhibited normal degradation (Fig.3B, 3D-3E, Extended
273 Fig.3A, 3D-3E). Collectively, these findings indicate that degradation of ER
274 components under prolonged mTOR inhibition depends primarily on the core
275 autophagy machinery, rather than on specific ER-phagy receptors.
276
277 We next analyzed ER morphology in cells lacking essential autophagy genes. ER
278 translocation into autolysosomes and autolysosomal whorls were abolished in ATG2,
279 ATG5, ATG7 and ATG8-hexa knockout cells (Fig.3F-3I, Extended Fig.3F-3G, 3M-3P),
280 whereas ERphR-KO did not affect whorl formation (Fig.3J-3K, Extended Fig.3H-3I).
281 Consistent with the genetic data, ER puncta in wild-type cells were positive for LC3
282 (Extended Fig.3J-3L), and notably, they exhibited strong ATG9A signal—distinct from
283 conventional autophagosomes, which typically show weak ATG9A labeling[51,52]

284 (Fig.3L-3M). Triple labeling with BFP-LC3, mCherry-REEP5, and LAMP1-YFP
285 revealed two classes of puncta: (i) REEP5^{+}/LC3^{+}/LAMP1^{-} puncta representing free
286 whorls, and (ii) REEP5^{+}/LC3^{+}/LAMP1^{+} puncta corresponding to whorls enclosed
287 within autolysosomes (Fig.3N).
288
289 APEX2 labeling confirmed these observations at the ultrastructural level, revealing
290 LC3-positive autophagosomes, multilamellar whorls, and whorls enclosed within
291 autolysosomes (Fig.3O-3P). Together, these results establish that core autophagy
292 components are indispensable for whorl formation and turnover, whereas canonical ER-
293 phagy receptors play only a minor role.
294
295 Based on these findings, we designate these structures "autolamellasomes", reflecting
296 both their dependence on autophagy machinery and their distinctive multilamellar
297 morphology. This nomenclature also distinguishes them from classical ER whorls
298 generated under ER-stress conditions.
299
300 **Autolamellasomes Form via Autophagy-Dependent Assembly of ER Fragments**
301
302 We next sought to elucidate the cellular mechanism underlying autolamellasome
303 formation. Reasoning that expanding the ER might enhance autolamellasome
304 generation, we treated cells with oleic acid (OA), which is known to induce ER
305 membrane expansion[53,54], followed by prolonged mTOR inhibition (Fig.4A).
306 Unexpectedly, OA treatment alone caused the appearance of large ER patches in both
307 wild-type and autophagy-deficient (ATG2, ATG5, and ATG7-deficient) cells (Fig.4B).
308 Fluorescence recovery after photobleaching (FRAP) experiments showed rapid
309 recovery of mCherry-REEP5 signal within these patches, indicating lateral diffusion of
310 ER fragments across patch boundaries—a behavior reminiscent of liquid–liquid phase
311 separation (Extended Fig.4A-4B).
312

313 When prolonged mTOR inhibition was applied, wild-type cells readily formed
314 autolamellasomes (Fig.4B). Time-lapse imaging revealed that autolamellasomes
315 emerged from ER patches and subsequently translocated into autolysosomes (Extended
316 Fig.4C). In contrast, in autophagy-deficient cells, ER patches enlarged over time but
317 failed to generate autolamellasomes. Interestingly, two distinct patterns were observed
318 among the autophagy-deficient cell types: in ATG2- and ATG7-deficient cells,
319 autolamellasome formation was completely blocked, whereas ATG5-deficient cells
320 exhibited a moderate level of formation. OA treatment induced ER patch formation in
321 most wild-type and ATG2-deficient cells, but only in a subset of ATG7- or ATG5-
322 deficient cells. However, upon prolonged mTOR inhibition, nearly all autophagy-
323 deficient cells displayed enlarged ER patches (Fig.4C-4D). These observations suggest
324 that while ATG5 and ATG7 may negatively modulate OA-induced ER patch formation,
325 the core autophagy machinery is required to convert ER patches into autolamellasomes.
326
327 To further characterize the nature of ER patches, we performed correlative light and
328 electron microscopy (CLEM) in wild-type cells. CLEM revealed that these patches
329 consist of clustered ER fragments (Fig.4E), consistent with their rapid fluorescence
330 recovery after photobleaching. TEM analysis showed abundant autolamellasomes
331 either free in the cytoplasm or enclosed within autolysosomes in wild-type cells,
332 whereas autophagy-deficient cells accumulated disordered ER fragments instead
333 (Fig.4F-4G). APEX2 labeling of SEC61B confirmed that in wild-type cells,
334 autolamellasomes emerged directly from ER fragment clusters, reflecting the assembly
335 of ordered multilamellar structures from disordered ER components. In contrast, no
336 autolamellasome structures were detected in autophagy-deficient cells (Fig.4H-4I).
337
338 Together, these data demonstrate that autolamellasomes arise through the autophagy-
339 dependent assembly of ER fragments, with the core autophagy machinery orchestrating
340 their transformation from disordered ER clusters into organized multilamellar
341 structures.

342

343 **Basal Autolamellasome Formation Occurs Widely *In Vitro* and *In Vivo***

344

345 One of the defining ultrastructural features of lysosomes is the presence of internal
346 membrane whorls. This observation prompted us to ask whether these whorls might
347 originate from basal-level autolamellasome formation followed by lysosomal
348 engulfment. To test this hypothesis, we performed TEM and fluorescence microscopy
349 analyses across a wide range of immortalized cell lines, primary cultured cells, mouse
350 zygotes, and multiple mouse organs.

351

352 We found that both free autolamellasomes and autolamellasomes enclosed within
353 lysosomes are widely present under basal conditions. The abundance of these structures
354 varied considerably among cell types and tissues (Fig.5A-5I, Extended Fig.5A-5G). For
355 example, the number of autolamellasomes in U2OS cells was comparable to that
356 observed in NRK cells after prolonged mTOR inhibition, while mouse zygotes
357 displayed predominantly free autolamellasomes (Fig.5E-5F). This diversity highlights
358 the dynamic basal turnover of ER-derived membranes across physiological contexts.

359

360 Interestingly, we later realized that our use of NRK cells for mTOR inhibition
361 experiments was entirely serendipitous—chosen without prior knowledge that NRK
362 cells exhibit the lowest basal level of autolamellasomes among the lines examined. This
363 fortunate coincidence provided an unusually clean baseline for visualizing and
364 quantifying induced autolamellasome formation.

365

366 We next examined whether basal autolamellasome formation depends on autophagy
367 core genes. Under nutrient-rich conditions, ATG7-deficient cells showed a marked
368 reduction in autolamellasome number, though the effect was less dramatic than under
369 prolonged mTOR inhibition (Fig.5J-5L). This suggests that while autophagy
370 contributes substantially, additional mechanisms may also promote low-level

371 autolamellasome formation in an ATG7-independent manner.

372

373 Because chloroquine (CQ) inhibits lysosomal degradation and, in some contexts,
374 autophagosome-lysosome fusion[55], we next assessed its effect on autolamellasome
375 formation. CQ treatment robustly induced autolamellasome formation, as confirmed by
376 ER Tracker staining (Fig.5M-5N), TEM (Fig.5O-5P), cryo-tomography (Fig.5Q), and
377 APEX2 labeling of SEC61B and LC3 (Fig.5R). In wild-type cells, CQ caused massive
378 translocation of ER material into lysosomes, whereas in ATG2-, ATG5-, and ATG7-
379 deficient cells, this translocation was strongly reduced. In these autophagy-deficient
380 cells, lysosomes lacked intralysosomal whorls (Fig.5S-5W).

381

382 Together, these findings resolve a longstanding question in lysosome biology: the origin
383 of intralysosomal whorls. Our results demonstrate that these whorls arise from basal
384 autolamellasome formation and lysosomal incorporation, a constitutive process present
385 across diverse cell types and organisms. The serendipitous use of NRK cells, with their
386 exceptionally low basal activity, provided a natural "zero point" that made this
387 discovery possible.

388

389 ***In Vitro* Reconstitution of Autolamellasome and Autophagosome Budding**

390

391 We next sought to establish a cell-free system capable of reconstituting
392 autolamellasome budding *in vitro* in a manner dependent on autophagy core
393 components. The assay was conceptually adapted from the classic COPII-budding
394 assay developed by the Schekman and Novick laboratories, which uses permeabilized
395 (semi-intact) cells to study vesicle formation[56,57]. However, instead of collecting
396 released vesicles, we monitored the formation of autolamellasomes within
397 permeabilized cells by transmission electron microscopy (TEM).

398

399 In this assay, cells were first pretreated with oleic acid (OA) for 24 hours to expand the

ER network. They were then permeabilized with digitonin in reconstitution buffer, supplemented with an S150 cytosolic fraction, ATP, and GTP, followed by incubation at 30 °C for 6-8 hours. Control samples received reconstitution buffer and digitonin alone (Fig.6A-6B). To ensure complete permeabilization and cell death, we stained samples with Apotracker, propidium iodide (PI), and Cy5. Apotracker labeling confirmed phosphatidylserine exposure on the plasma membrane outer leaflet, Cy5 positivity indicated membrane permeabilization, and PI nuclear staining verified loss of nuclear membrane integrity—together confirming that all treated cells were fully permeabilized and non-viable (Extended Fig.6A-6D, Extended Fig.6-6O).

To assess lysosomal integrity, we used Magic Red and Lysotracker staining. Both signals were abolished following digitonin treatment, indicating lysosomal disruption. Besides, microtubule integrity was also destroyed—a condition expected to facilitate the observation of free autolamellasomes (Extended Fig.6E-6H, 6J-6M).

TEM analysis revealed striking differences between control and reconstituted samples. In control preparations, internal membrane structures were extensively disrupted. In contrast, samples containing cytosol and nucleotides displayed numerous autolamellasomes at various stages of formation, as well as autophagosomes (Fig.6C-6E). Compared with TEM analysis of intact cells, the proportion of free autolamellasomes was substantially increased, suggesting efficient reconstitution of their formation within permeabilized cells.

We next examined the dependence on ATG7. Using ATG7-deficient cells as the membrane source, addition of wild-type S150 cytosol partially rescued autolamellasome formation to ~60 % of wild-type efficiency. Surprisingly, cytosol derived from ATG7-deficient cells still supported low-level formation—about one-third of wild-type levels—indicating that while ATG7 is indispensable for autolamellasome formation *in vivo*, limited assembly can occur *in vitro* (Fig.6F-6H). Together, these

429 results establish a foundational cell-free system that captures the essential process of
430 autolamellasome and autophagosome biogenesis. This *in vitro* approach reveals a core
431 mechanistic principle: the formation of these structures is driven by soluble cytosolic
432 factors acting upon permeabilized cellular membranes. Furthermore, the system
433 demonstrates that while the core component ATG7 is a major accelerator of
434 autolamellasome formation, the process retains a basal, ATG7-independent capacity.
435 This suggests the existence of either alternative, low-efficiency pathways or a residual
436 self-organizing potential within the membrane itself that can be co-opted by the cytosol
437 to initiate this form of membrane remodeling.
438
439 **Induction of Autolamellasomes in Senescent Cells and Cells from Premature-**
440 **Aging Patients**
441
442 Lysosomal activity is known to decline with age in both animals and humans[58]. To test
443 whether autolamellasomes accumulate in senescent cells, we employed two well-
444 established models of cellular senescence: doxorubicin-induced DNA damage[59] and
445 tert-butyl hydroperoxide (TBHP)-induced oxidative stress[60]. Senescence was
446 confirmed by SA–β-galactosidase staining, which showed robust activity in both
447 models (Fig.7A-C, Extended Fig.7B-7D).
448
449 Transmission electron microscopy (TEM) and fluorescence imaging revealed a
450 dramatic accumulation of autolamellasomes in senescent cells, whereas autophagy-
451 deficient cells failed to form autolamellasomes and instead accumulated large, irregular
452 ER patches (Fig.7F-7L, Extended Fig.7A, Extended Fig.7G-7M). Interestingly, mTOR
453 activity was largely suppressed in both senescence models (Fig.7D-E, Extended Fig.7E-
454 7F). Moreover, treatment with MHY1485—a small-molecule activator of mTOR—
455 effectively prevented ER translocation into autolysosomes (Fig.7M-7N). Collectively,
456 these findings mechanistically explain enhanced autolamellasome formation under
457 mTOR inhibition, suggesting that their accumulation in senescent cells results from

both reduced lysosomal degradation capacity and active induction via mTOR inhibition.

To further explore this phenomenon in the context of genetic premature aging, we analyzed human dermal fibroblasts (HDFs) derived from Hutchinson-Gilford Progeria Syndrome (HGPS) patients[61]—a rare laminopathy that causes severe premature aging in children. Compared with HDFs from healthy individuals, HGPS fibroblasts displayed markedly increased autolamellasome accumulation (Fig.7O-7R) and reduction of mTOR activity (Fig.7S-7T). HGPS arises from a mutation in the LMNA gene, which encodes lamin A; this mutation produces a truncated, farnesylated form known as progerin, leading to nuclear envelope deformation and global cellular stress[62].

To directly test the role of progerin, we established a doxycycline-inducible progerin-expressing cell line. Induction of progerin expression led to robust formation of autolamellasomes, whereas this response was completely abolished in autophagy-deficient cells, confirming that autolamellasome formation is autophagy-dependent (Fig.7U-7W, Extended Fig.7N).

Together, these findings position autolamellasome accumulation as a conserved cellular signature of aging, emerging at the intersection of declining lysosomal function and persistent ER stress. Rather than a passive breakdown, this process represents an active, autophagy-dependent remodeling pathway, triggered by the near-universal age-associated suppression of mTOR. This pathway thus links core hallmarks of aging—dysfunctional organelles and nutrient signaling collapse—into a unified, structural adaptation.

Discussion

This study uncovers a previously unrecognized form of ER remodeling that operates under conditions of chronic mTOR inhibition. We identify autolamellasomes, multilamellar ER-derived structures that arise through the core autophagy machinery

but independently of canonical ER-phagy receptors. Unlike conventional autophagosomes, autolamellasomes mediate bulk ER degradation via autophagy-dependent assembly and lysosomal incorporation of compacted ER fragments. Their presence across multiple cell types, and their accumulation in senescent and HGPS fibroblasts, reveal a conserved, aging-associated remodeling pathway linking sustained mTOR suppression to ER and lysosomal homeostasis. These findings redefine how long-term autophagy activation reshapes cellular architecture, providing a structural and mechanistic framework that connects nutrient-sensing, membrane dynamics, and aging.

Beyond revealing a new mode of ER turnover, our findings also resolve a long-standing question in cell biology—the origin of the membrane whorls long observed within lysosomes. These enigmatic multilamellar structures, variably termed myelin figures or zebra bodies, have been described for decades in electron microscopy studies but lacked a defined biogenic pathway. Our data demonstrate that these intralysosomal whorls originate from basal autolamellosome formation, followed by lysosomal incorporation. Importantly, autolamellasomes are not restricted to experimental mTOR inhibition but are constitutively generated at low levels across a wide range of cell types and tissues, from cultured mammalian cells to mouse embryos. This basal activity likely represents a housekeeping mechanism that continuously remodels the ER and contributes to the steady-state membrane flux through lysosomes. Thus, the identification of autolamellasomes provides a unifying explanation for the biogenesis of lysosomal membrane whorls and establishes a physiological link between ER dynamics, lysosome structure, and long-term membrane homeostasis.

The autolamellosome pathway is mechanistically distinct from previously described ER-derived whorls in both yeast and mammalian systems. In *Saccharomyces cerevisiae*, ER whorls form rapidly under acute ER stress and are degraded through a specialized micro-ER-phagy route. This process involves direct invagination of the vacuolar

membrane, followed by ESCRT-mediated scission to internalize the whorl. It proceeds independently of the core ATG machinery and canonical ER-phagy receptors, relying instead on vacuolar sorting components and the ER-localized Nem1-Spo7 phosphatase complex, which regulates phosphatidic acid turnover and membrane curvature. In contrast, the ER-stress-induced whorls in mammalian cells—large, concentric stacks up to several micrometers in diameter—arise through a PERK- and COPII-dependent remodeling program that serves an adaptive function: concentrating PERK and sequestering translocons to transiently dampen protein import during stress. These structures are not degraded via autophagy, but rather disassembled upon stress resolution, and their biogenesis is tightly coupled to the unfolded protein response (UPR) signaling network. By contrast, autolamellosomes emerge under sustained mTOR inhibition and depend on the core autophagy machinery but not ER-phagy receptors or UPR signaling. They represent a degradative remodeling route that links nutrient sensing to long-term membrane recycling, distinguishing them from both the ESCRT-dependent ER whorl degradation in yeast and PERK-driven ER whorl formation in mammalian.

A key advance of this study is the establishment of a cell-free reconstitution system that faithfully recapitulates autolamellasome formation *in vitro*. This approach demonstrates that multilamellar ER structures can self-organize from cellular membranes in response to soluble cytosolic factors and energy cofactors, revealing that the core autophagy machinery is sufficient to drive their assembly. The significance of this finding extends far beyond the specific phenomenon described here: cell-free reconstitution has historically been pivotal in cell biology, transforming abstract cellular processes into experimentally tractable biochemical reactions. Seminal examples include the reconstitution of COPII- and COPI-coated vesicle budding from the ER and Golgi membranes—discoveries that defined the molecular logic of vesicular trafficking. By establishing a comparable system for autolamellosome biogenesis, our work brings this newly identified pathway into the same mechanistic framework, enabling its dissection at molecular resolution. This cell-free system provides not only proof of principle that

autolamellosome formation is a bona fide, self-organizing process but also a powerful platform for future biochemical and structural reconstitution of autophagy-driven membrane remodeling.

Despite elucidating the existence and mechanistic basis of autolamellosome formation, our study has several important limitations that point to future directions. The specific molecular components that distinguish this pathway from canonical autophagy remain unknown. Although the core autophagy machinery is essential, additional factors likely confer the multilamellar morphology and ER specificity of autolamellosomes. A comprehensive whole-genome CRISPR or siRNA screen will be critical to identify such unique regulators, including membrane-shaping or lipid-metabolizing proteins. Moreover, the physiological significance of autolamellosomes requires validation *in vivo*. Developing animal models that allow controlled modulation of autolamellosome formation will enable investigation of their roles in organ function, stress adaptation, and organismal physiology. Given their capacity for extensive membrane remodeling and lipid catabolism, autolamellosomes may serve as an adaptive mechanism for energy recycling during prolonged nutrient limitation. Their pronounced accumulation in senescent and progeroid cells further suggests that this pathway participates in the cellular response to aging-associated mTOR suppression and lysosomal decline. Because chronic mTOR dysregulation, ER stress, and impaired lipid homeostasis are hallmarks of diverse human disorders—including metabolic diseases, neurodegeneration, and cancer—autolamellosome formation may represent a broader protective or maladaptive remodeling response in these contexts. Future studies integrating unbiased genetic screening, *in vitro* reconstitution, disease modeling, and physiological analyses will be essential to define how autolamellosomes contribute to membrane homeostasis, metabolic resilience, aging, and disease pathogenesis.

Figures and figure legends

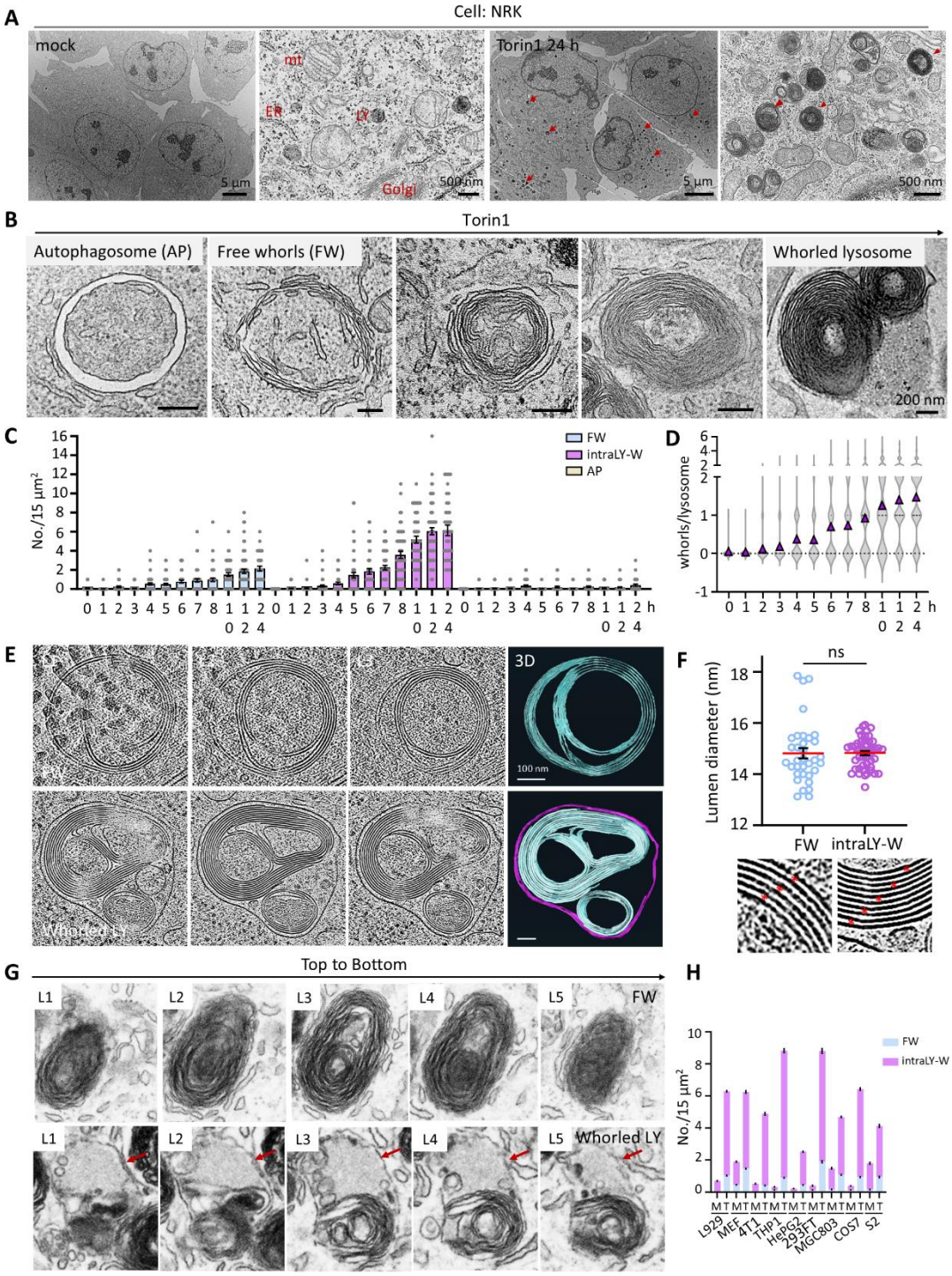

Figure 1 Prolonged mTOR inhibition induces the formation of "free whorls". (A) Representative TEM images of NRK cells treated with or without 1 μM Torin1 for 24 h. Red arrows indicate electron-dense whorls. ER: the endoplasmic reticulum; mt: mitochondria; LY: lysosome; Golgi: Golgi apparatus. Scale bars: 5 μm (overview) or 500 nm (magnified view).

579 (B) Representative TEM images of autophagosome (AP), free whorls (FW) at different
580 stages and lysosome/autolysosome containing with whorls (Whorled lysosome). NRK
581 cells were treated with 1 μM Torin1 for a time series. Scale bars, 200 nm.
582 (C) TEM images from (B) were quantified for the amount of each kind of structure (FW:
583 free whorls, intraLY-W: intralysosomal whorls, AP: autophagosome) in 15 μm^2 area.
584 For each time point, more than 38 cells were imaged. Data are reported as mean ± SEM.
585 (D) TEM images from (B) were quantified for the number of whorls contained in each
586 lysosome/autolysosome. For each time point, more than 70 lysosomes/ autolysosomes
587 were quantified. Data are presented as violin plots showing the full distribution, with
588 the mean indicated by a triangle.
589 (E) Representative cryo-ET (cryo-electron tomography) images and 3D rendered
590 images of free whorl (FW) and lysosome/autolysosome containing with whorls
591 (Whorled lysosome) in NRK cells treated with 1 μM Torin1 for 24 h. L1-L3 indicated
592 different layers of the structure. Scale bars, 100 nm.
593 (F) Lumen diameter of the whorls from (E) were quantified. Data are reported as mean
594 ± SEM. n=34 for FW group, n=48 for intraLY-W group. ns, not significant. P values
595 were calculated using a two-tailed, unpaired t test. Asterisks indicated the lumens of
596 whorls.
597 (G) Representative FIB (focused ion beam) images of free whorl (FW) and
598 lysosome/autolysosome containing with whorls (Whorled lysosome). L1-L5 indicated
599 different layers of the structure.
600 (H) Quantification of free whorls (FW) and intralysosomal whorls (intraLY-W) from
601 TEM images of multiple cell lines treated with 1 μM Torin1 for 24 h. M, mock; T,
602 Torin1. Sample sizes (n) were as follows: L929 (M: n=40; T: n=68), MEF (M: n=78;
603 T: n=56), 4T1 (M: n=54; T: n=34), THP1 (M: n=43; T: n=46), HepG2 (M: n=74; T:
604 n=54), 293FT (M: n=32; T: n=29), MGC803 (M: n=35; T: n=38), COS7 (M: n=64; T:
605 n=49), and S2 (M: n=25; T: n=31).

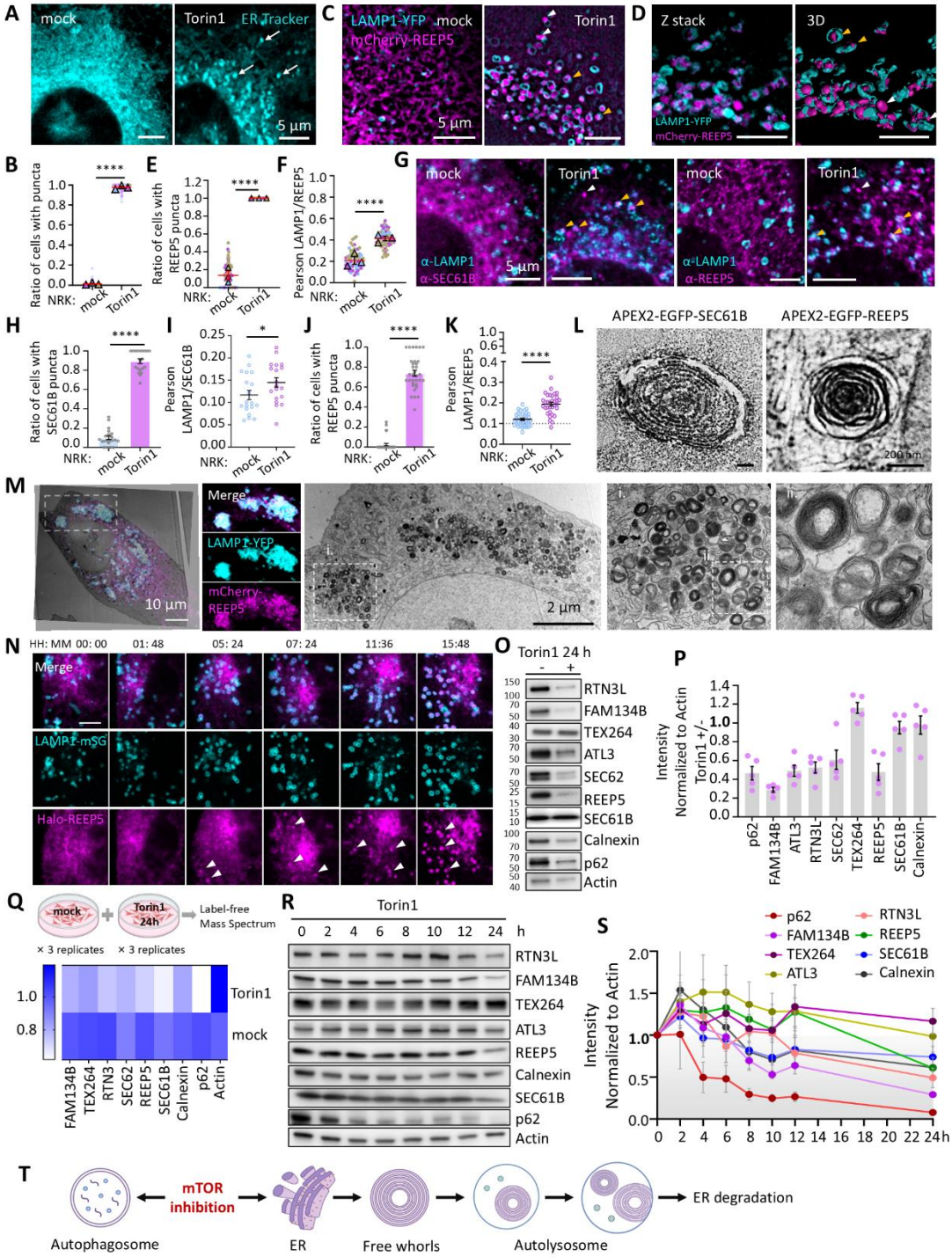

Figure 2 Whorls originate from the Endoplasmic Reticulum.

(A) Representative confocal images of NRK cells treated with or without 1 μM Torin1 for 24 h. NRK cells were labeled by ER Tracker. Arrows indicate ER puncta. Scale bars, 5 μm.

(B) Quantification of the ratio of cells shown in (A) contained with ER puncta. More

612 than 230 cells were analyzed per group in each experiment (n=3 experiments). Error
613 bars indicate mean ± SEM. ****, p<0.0001. P values were calculated using a two-tailed,
614 unpaired t test.
615 (C) Representative SIM images of NRK cells stably co-expressing LAMP1-YFP and
616 mCherry-REEP5 treated with or without 1 μM Torin1 for 24 h. White arrows: free-
617 standing ER puncta, yellow arrows: ER puncta inside lysosomes. Scale bars, 5 μm.
618 (D) Representative z-stack image and its 3D rendered image of cells from (C). Scale
619 bars, 5 μm.
620 (E-F) Quantification of the cells shown in (B). (E) Ratio of cells with mCherry-REEP5
621 labeled-ER puncta. (F) Pearson correlation coefficient of LAMP1-YFP and mCherry-
622 REEP5 signals. More than 135 cells were analyzed per group in each experiment (n=3
623 experiments). Error bars indicate mean ± SEM. ****, p<0.0001. P values were
624 calculated using a two-tailed, unpaired t test.
625 (G) Endogenous immunostaining of NRK cells treated with or without 1 μM Torin1 for
626 24 h. Cells were stained with anti-LAMP1/anti-SEC61B and anti-LAMP1/anti-REEP5
627 antibodies. White arrows: free-standing ER puncta, yellow arrows: ER puncta inside
628 lysosomes. Scale bars, 5 μm.
629 (H-K) Quantification of the cells shown in (G). (H) Ratio of cells with SEC61B labeled-
630 ER puncta. (I) Pearson correlation coefficient of LAMP1 and SEC61B signals. (J) Ratio
631 of cells with REEP5 labeled-ER puncta. (K) Pearson correlation coefficient of LAMP1
632 and REEP5 signals. More than 180 cells were analyzed per condition. Error bars
633 indicate mean ± SEM. *, p<0.05, ****, p<0.0001. P values were calculated using a
634 two-tailed, unpaired t test.
635 (L) Representative APEX2-TEM images of free whorls in NRK cells stably expressing
636 APEX2-EGFP-SEC61B or APEX2-EGFP-REEP5 treated with Torin1. Scale bar, 200
637 nm.
638 (M) CLEM data of NRK cells stably co-expressing LAMP1-YFP and mCherry-REEP5
639 treated with Torin1. The marked region in the fluorescent graph stacked with the
640 electron microscope graph was enlarged and demonstrated on the right. Scale bars

641 denoted 10 μm for the stacked graph, 2 μm for the electron microscope graph.
642 (N) Time-lapse live cell images of NRK cells stably co-expressing LAMP1-mStaygold
643 and HaloTag-REEP5 treated with Torin1. Here shows representative snapshots at
644 indicated time points. Scale bar, 5 μm.
645 (O) Western blot results of NRK cells treated with or without 1 μM Torin1 for 24 h.
646 Cell lysates were subjected to SDS-PAGE and immunoblotted with the indicated
647 antibodies. Blots are representative of n=5 independent biological replicates.
648 (P) Quantification of integrated band intensities from (O). Individual data points
649 represent relative protein levels in the Torin1-treated group normalized to the untreated
650 control and loading control Actin. n=5 independent biological repeats. Data are
651 presented as mean ± SEM.
652 (Q) Heatmap of relative protein abundances measured by label-free mass spectrometry
653 in NRK cells treated with or without 1 μM Torin1 for 24 h. Values were normalized to
654 the mock-1 group. n=3 independent biological repeats. Color scale indicates fold
655 change relative to mock-1 group.
656 (R) Western blot results of NRK cells treated with 1 μM Torin1 in a time series. Cell
657 lysates were subjected to SDS-PAGE and immunoblotted with the indicated antibodies.
658 Blots are representative of n=4 independent biological replicates.
659 (S) Quantification of integrated band intensities from (R). Individual data points
660 represent relative protein levels in the time point normalized to 0 h and loading control
661 Actin. n=4 independent biological repeats. Data are presented as mean ± SEM.
662 (T) Schematic diagram illustrating that mTOR inhibition stimulates parallel formation
663 of autophagosomes and free whorls.

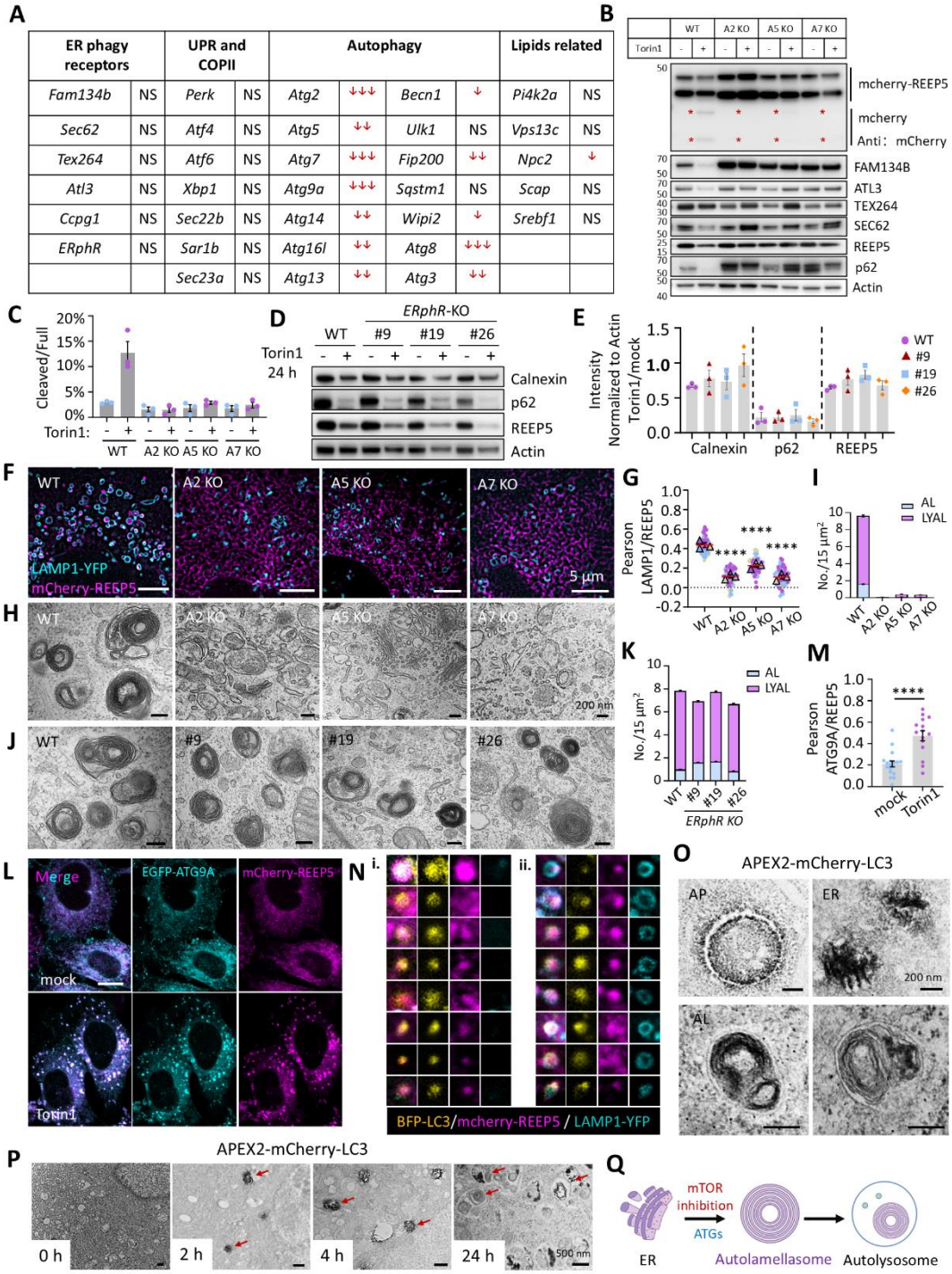

Figure 3 Formation of whorls depends on the core autophagy machinery but not ER-phagy receptors.

(A) Table of knockout genes and their effects on whorls formation. *ERphR*: ER phagy receptor penta KO. ↓ slightly decrease，↓↓ moderated decease, ↓↓↓ almost disappear. (B) Western blot analysis of endogenous proteins and mCherry cleavage in WT and

670 autophagy-deficient NRK cells. WT, *Atg2* KO, *Atg5* KO, *Atg7* KO NRK cells were
671 treated with or without 1 μM Torin1 for 24 h. Cell lysates were subjected to SDS-PAGE
672 and immunoblotted with the indicated antibodies. Asterisks denote cleaved mCherry
673 fragments generated upon autophagic degradation. Actin served as a loading control.
674 Blots are representative of n=3 independent biological replicates.
675 (C) Quantification of mCherry-REEP5 cleavage. The percentage of cleaved mCherry
676 fragments relative to full-length mCherry-REEP5 was quantified from the Western blot
677 shown in (B). Data are presented as mean ± SEM from n=3 independent biological
678 replicates.
679 (D) Western blot analysis of *ERphR* KO (ER-phagy receptor penta-KO) clones.
680 Wild-type (WT) and three independent *ERphR* KO NRK cell clones (#9, #19, #26) were
681 treated with or without 1 μM Torin1 for 24 h. Cell lysates were subjected to SDS-PAGE
682 and immunoblotted with the indicated antibodies. Blots are representative of n=3
683 independent biological replicates.
684 (E) Quantification of integrated band intensities from (D). Individual data points
685 represent relative protein levels in the Torin1-treated group normalized to the untreated
686 control and loading control Actin. n=3 independent biological repeats. Data are
687 presented as mean ± SEM.
688 (F) Wild-type (WT) and autophagy-deficient NRK cells (*Atg2* KO, *Atg5* KO, or *Atg7*
689 KO, as indicated) stably co-expressing LAMP1-YFP and mCherry-REEP5 were treated
690 with 1 μM Torin1 for 24 h. Cells were imaged by Structured Illumination Microscopy
691 (SIM). Scale bars, 5 μm.
692 (G) Pearson correlation coefficient of LAMP1 and REEP5 signals of the cells shown in
693 (F). More than 300 cells were analyzed for each group (n=3 independent biological
694 repeats). Error bars indicate mean ± SEM. ****, $p<0.0001$. P values were calculated
695 using a two-tailed, unpaired t test.
696 (H) Representative TEM images of WT and autophagy-deficient (*Atg2* KO, *Atg5* KO,
697 or *Atg7* KO, as indicated) NRK cells treated with 1 μM Torin1 for 24 h. Scale bars, 200
698 nm.

699 (I) TEM images from (H) were quantified for the amount of each kind of structure (AL:
700 autolamellasome, LYAL: lysosome/autolysosome containing with autolamellasome) in
701 15 μm^2 area. More than 37 cells were imaged for each group. Data are reported as mean
702 ± SEM.
703 (J) Representative TEM images of WT NRK and *ERphR* KO clones treated with 1 μM
704 Torin1 for 24 h. Scale bars, 200 nm.
705 (K) TEM images from (J) were quantified for the amount of each kind of structure (AL:
706 autolamellasome, LYAL: lysosome/autolysosome containing with autolamellasome) in
707 15 μm^2 area. More than 43 cells were imaged for each group. Data are reported as mean
708 ± SEM.
709 (L) Representative confocal images of NRK cells stably co-expressing EGFP-ATG9A
710 and mCherry-REEP5 treated with or without 1 μM Torin1 for 24 h. Scale bar, 5 μm.
711 (M) Pearson correlation coefficient of ATG9A and REEP5 signals of the cells shown
712 in (L). More than 150 cells were analyzed for each group. Error bars indicate mean ±
713 SEM. ****, $p<0.0001$. P values were calculated using a two-tailed, unpaired t test.
714 (N) Representative confocal images of NRK cells stably co-expressing BFP-LC3,
715 mCherry-REEP5 and LAMP1-YFP treated with Torin1. (i) Representative images of
716 BFP-LC3$^+$/mCherry-REEP5$^+$/LAMP1-YFP$^-$ puncta, corresponding to LC3 labeled free
717 ER. (ii) Representative images of BFP-LC3$^+$/mCherry-REEP5$^+$/LAMP1-YFP$^+$ ER
718 puncta, indicating ER in lysosomes.
719 (O) Representative APEX2-TEM images of cells stably expressing APEX2-mCherry-
720 LC3 NRK cells treated with 1 μM Torin1. APEX2 labeled autophagosome (AP), the
721 endoplasmic reticulum (ER), autolamellasome (AL) are shown here as indicated. Scale
722 bars, 200 nm.
723 (P) NRK cells stably expressing APEX2-mCherry-LC3 were treated with 1 μM Torin1
724 and processed for APEX2-TEM at the indicated time points. Red arrows mark
725 LC3-positive structures. Scale bars, 500 nm.
726 (Q) Schematic diagram illustrating that autophagy genes (ATGs) are key regulators of
727 autolamellasome formation.

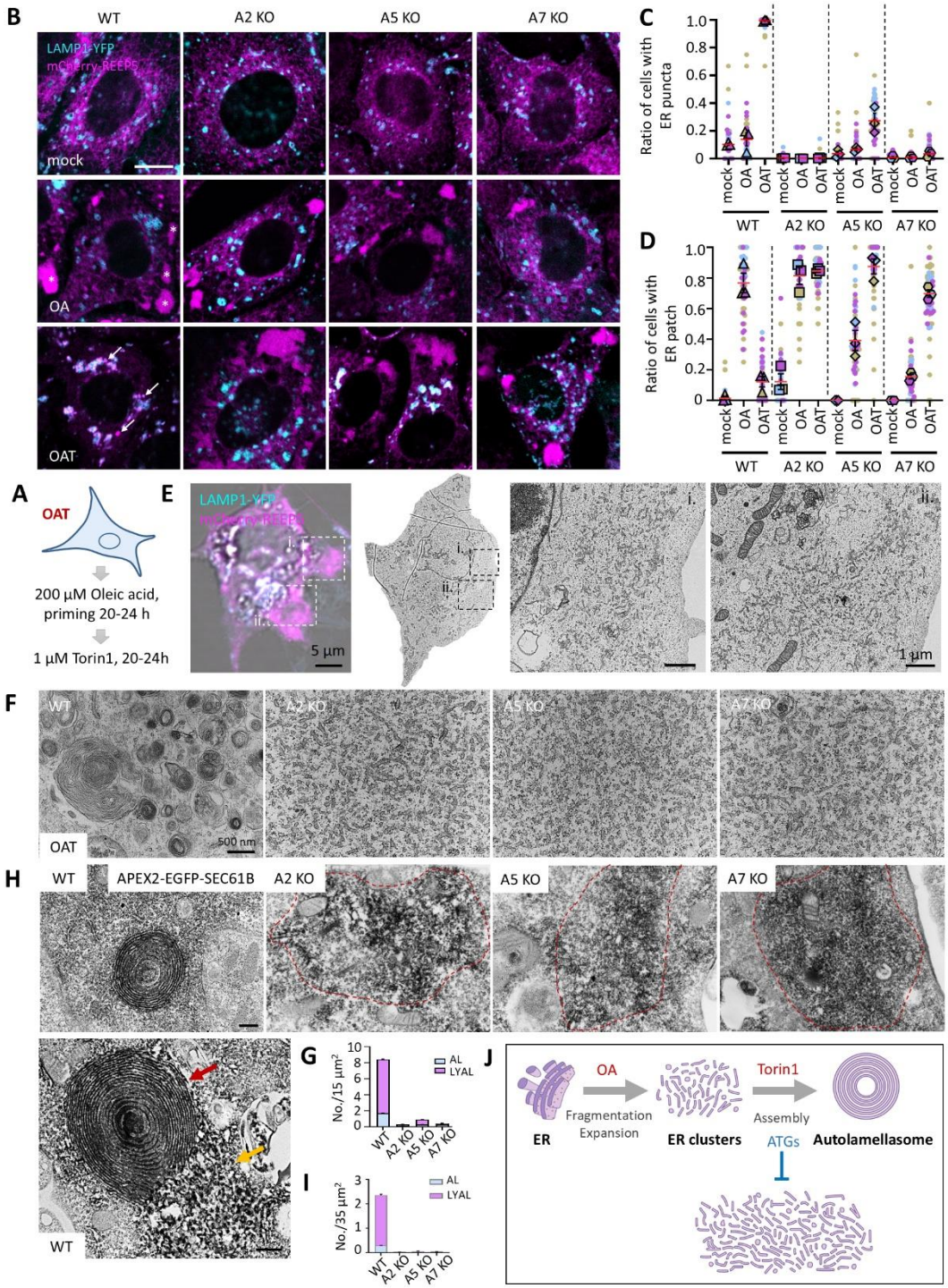

Figure 4 Autolamellasome formation via autophagy-dependent assembly of ER fragements

(A) Schematic diagram of the sequential drug treatment protocol in NRK cells. NRK cells were primed with 200 μM oleic acid (OA) for the initial incubation period, followed by direct supplementation with 1 μM Torin1 for further treatment (OAT).

734 (B) Wild-type (WT) and autophagy-deficient NRK cells (*Atg2* KO, *Atg5* KO, or *Atg7*
735 KO, as indicated) stably co-expressing LAMP1-YFP and mCherry-REEP5 were treated
736 with 200 μM oleic acid (OA) for 24 h, or OA followed by 1 μM Torin1. Cells were
737 imaged by confocal microscopy. Arrows indicate ER puncta while asterisks indicate
738 ER patches. Scale bar, 5 μm.
739 (C-D) Quantification of cells from (B). (C) Statistics of the ratio of cells with ER puncta.
740 (D) Statistics of the ratio of cells with ER patches. More than 70 cells were analyzed
741 for each group (n=3 independent biological repeats). Error bars indicate mean ± SEM.
742 (E) CLEM data of NRK-*Atg7*-KO cells stably expressing LAMP1-YFP/mCherry-
743 REEP5 treated with OAT. The marked region was enlarged and demonstrated on the
744 right. Scale bars denoted 5 μm for the fluorescence graph, 1 μm for the electron
745 microscope graph.
746 (F) Representative TEM images of WT and autophagy-deficient NRK cells treated
747 OAT. Scale bar, 500 nm.
748 (G) TEM images from (F) were quantified for the amount of each kind of structure (AL:
749 autolamellasome, LYAL: lysosome/autolysosome containing with autolamellasome) in
750 15 μm^2 area. More than 60 cells were imaged for each group. Data are reported as mean
751 ± SEM.
752 (H) Representative APEX2-TEM images of WT and autophagy-deficient NRK cells
753 stably expressing APEX2-EGFP-SEC61B and treated with OAT. Red dashed lines
754 indicate clusters of ER fragments. Red arrow indicates autolamellasome, yellow arrow
755 indicates ER fragments. Scale bars, 500 nm.
756 (I) TEM images from (H) were quantified for APEX2-postive structures (AL:
757 autolamellasome, LYAL: lysosome/autolysosome containing with autolamellasome) in
758 35 μm^2 area. More than 50 cells were imaged for each group. Data are reported as mean
759 ± SEM.
760 (J) Schematic diagram illustrating oleic acid (OA)-induced clustering of ER fragments
761 and subsequent Torin1-driven, autophagy-dependent autolamellasome formation.

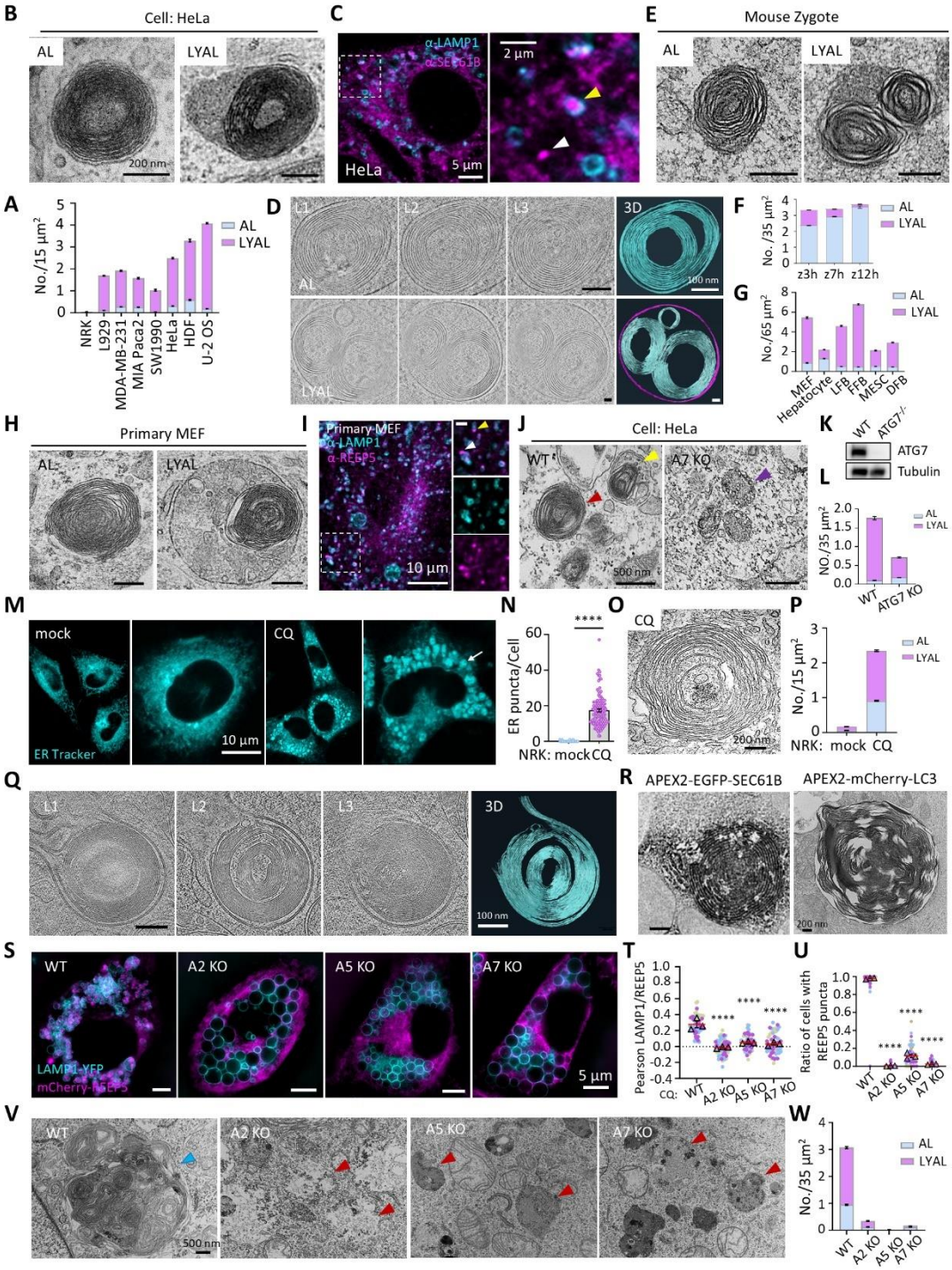

Figure 5 Widespread basal autolamellasome formation *in vitro* and *in vivo*.

(A) Quantification of AL (autolamellasome) and LYAL (lysosome/autolysosome containing with autolamellasome) number per 15 μm^2 area from TEM images for each indicated cell line. More than 30 cells were analyzed per group. Data are reported as mean ± SEM.

768 (B) Representative TEM images of AL (autolamellasome) and LYAL
769 (lysosome/autolysosome containing with autolamellasome) in HeLa cells. Scale bars,
770 200 nm.
771 (C) HeLa cells were co-stained with anti-LAMP1/anti-SEC61B antibodies. White
772 arrow: free-standing ER puncta, yellow arrow: ER puncta inside lysosomes. Scale bars:
773 5 μm (main image) and 2 μm (magnified view).
774 (D) Representative cryo-ET images and 3D rendered images of AL (autolamellasome)
775 and LYAL (lysosome/autolysosome containing with autolamellasome) in HeLa cells.
776 L1-L3 indicated different layers of the structure. Scale bars, 100 nm.
777 (E) Representative TEM images of AL (autolamellasome) and LYAL
778 (lysosome/autolysosome containing with autolamellasome) in mouse zygotes. Scale
779 bars, 200 nm.
780 (F) Quantification of AL (autolamellasome) and LYAL (lysosome/autolysosome
781 containing with autolamellasome) number per 35 μm^2 area from (E). Mouse zygotes
782 were collected at 3, 7, and 12 hours and imaged. n = 3 (z3h), n = 3 (z7h), and n = 2
783 (z12h). Data are reported as mean ± SEM.
784 (G) Quantification of AL (autolamellasome) and LYAL (lysosome/autolysosome
785 containing with autolamellasome) number per 65 μm^2 area from TEM images for each
786 indicated primary cell. More than 35 cells were analyzed per group. Data are reported
787 as mean ± SEM.
788 (H) Representative TEM images of AL (autolamellasome) and LYAL
789 (lysosome/autolysosome containing with autolamellasome) in primary MEF cells.
790 Scale bars, 200 nm.
791 (I) Primary MEF cells were co-stained with anti-LAMP1/anti-REEP5 antibodies. White
792 arrow: free-standing ER puncta, yellow arrow: ER puncta inside lysosomes. Scale bars:
793 10 μm (main image) and 2 μm (magnified view).
794 (J) Representative TEM images of WT and ATG7 KO HeLa cells. Scale bars, 500 nm.
795 (K) Validation of knockout efficiency of ATG7 KO HeLa cells via Western blot.
796 (L) Quantification of AL (autolamellasome) and LYAL (lysosome/autolysosome

797 containing with autolamellasome) number per 35 μm^2 area from (J). More than 50 cells
798 were analyzed per group. Data are reported as mean ± SEM.
799 (M) Representative confocal images of NRK cells treated with or without 100 nM
800 chloroquine (CQ) for 18 h. Arrow indicates ER Tracker-labeled puncta. Scale bar, 5
801 μm.
802 (N) Quantification of the number of ER puncta per cell in cells shown in (M). More
803 than 120 cells were analyzed per group. Error bars indicate mean ± SEM. ****,
804 $p<0.0001$. P values were calculated using a two-tailed, unpaired t test.
805 (O) Representative TEM images of NRK cells treated with 100 nM chloroquine (CQ)
806 for 18 h. Scale bar, 200 nm.
807 (P) Quantification of AL (autolamellasome) and LYAL (lysosome/autolysosome
808 containing with autolamellasome) number per 15 μm^2 area from (O). More than 65 cells
809 were analyzed per group. Data are reported as mean ± SEM.
810 (Q) Representative cryo-ET (cryo-electron tomography) images and 3D rendered
811 images of autolamellasome (AL) and lysosome/autolysosome containing with
812 autolamellasome (LYAL) in NRK cells treated with 100 nM chloroquine (CQ) for 18
813 h. L1-L3 indicated different layers of the structure. Scale bars, 100 nm.
814 (R) Representative APEX2-TEM images of autolamellasomes in NRK cells stably
815 expressing APEX2-EGFP-SEC61B or APEX2-mCherry-LC3. Cells were treated with
816 100 nM chloroquine (CQ) for 18 h. Scale bars, 200 nm.
817 (S) Representative SIM images of WT and autophagy-deficient NRK cells stably co-
818 expressing LAMP1-YFP and mCherry-REEP5. Cells were treated with 100 nM CQ for
819 18 h. Scale bars, 5 μm.
820 (T-U) Quantification of the cells shown in (S). (T) Pearson correlation coefficient of
821 LAMP1 and REEP5 signals. (U) Ratio of cells with ER puncta. More than 140 cells
822 were analyzed in each group for each experiment (n=3 independent biological repeats).
823 Error bars indicate mean ± SEM. ****, $p<0.0001$. P values were calculated using a two-
824 tailed, unpaired t test.
825 (V) Representative TEM images of WT and autophagy-deficient NRK cells stably co-

826 expressing LAMP1-YFP/mCherry-REEP5. Cells were treated with 100 nM CQ for 18
827 h. Blue arrow: autolamellasomes. Red arrows: lysosomes. Scale bar, 500 nm.
828 (W) Quantification of AL (autolamellasome) and LYAL (lysosome/autolysosome
829 containing with autolamellasome) number per 35 μm^2 area from (V). More than 40 cells
830 were analyzed per group. Data are reported as mean ± SEM.
831

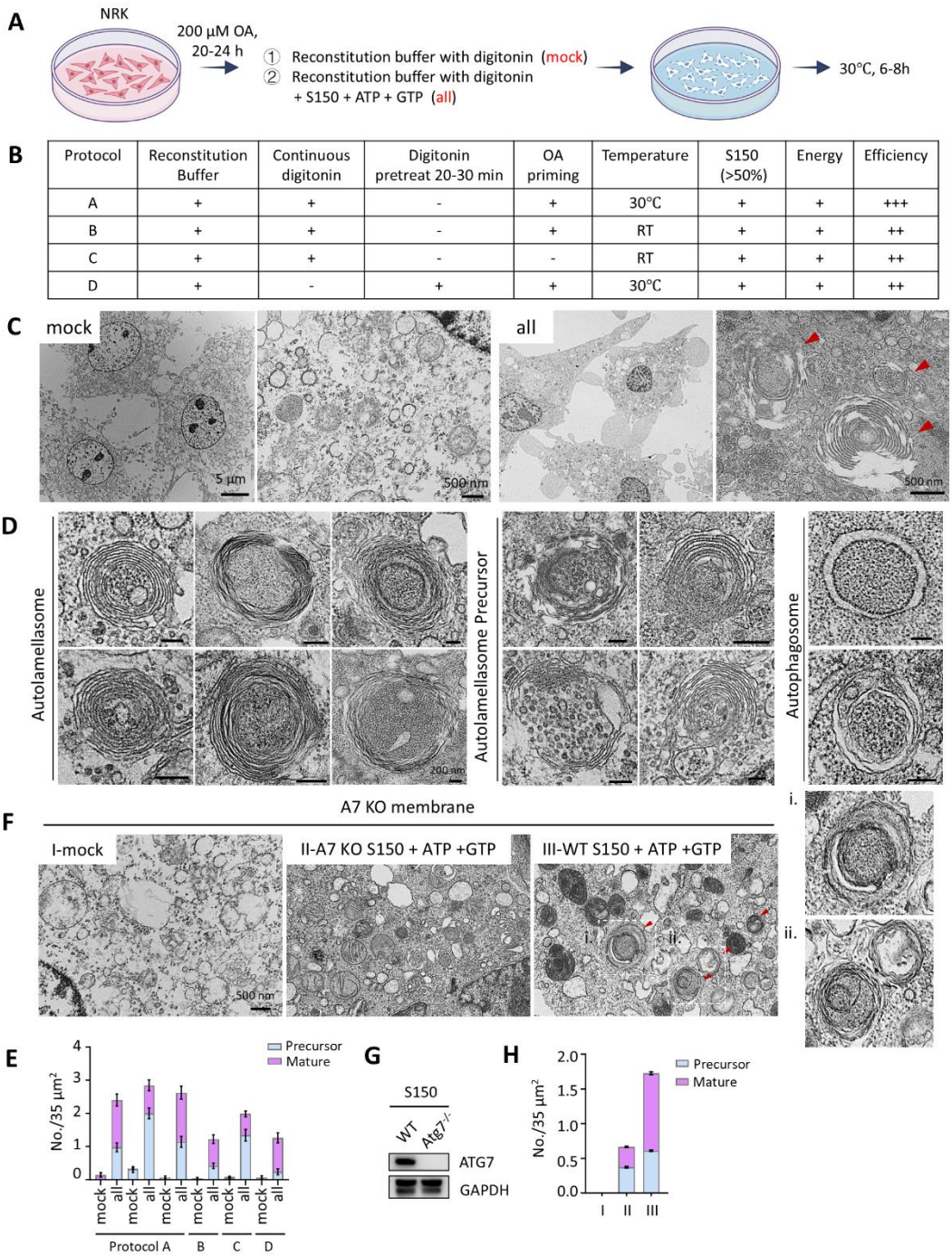

Protocol	Reconstitution Buffer	Continuous digitonin	Digitonin pretreat 20-30 min	OA priming	Temperature	S150 (>50%)	Energy	Efficiency
A	+	+	-	+	30℃	+	+	+++
B	+	+	-	+	RT	+	+	++
C	+	+	-	-	RT	+	+	++
D	+	-	+	+	30℃	+	+	++

Figure 6 *In vitro* reconstitution of autolamellasome.

(A) Schematic diagram illustrating the process of *in vitro* reconstitution of autolamellasome. NRK cells were primmed with 200 μM OA for 20-24 h, followed by incubation in reconstitution buffer containing 40 μg/mL digitonin (mock group) or supplemented with S150, ATP and GTP (all group) for 6-8 h at 30 ℃.

(B) Table of various protocols for *in vitro* autolamellasome reconstitution and their

839 efficiencies.

840 (C) Representative TEM images of membrane structures in mock group and all group
841 from protocol A. Red arrows indicated autollamellasome-like structures. Scale bar=5
842 μm for large view. Scale bar=500 nm for magnified view.

843 (D) Representative TEM images of autollamellasomes, autollamellasome precursors
844 and autophagosomes in all group. Scale bars, 200 nm.

845 (E) Quantification of sealed mature autolamellasomes (Mature) and unsealed
846 autolamellasome precursors (Precursor) in the *in vitro* reconstitution system using
847 different protocols. Protocol A: n=3 independent biological repeats, >35 fields of view
848 per group per experiment. Protocols B, C, and D: >30, >50, and >40 fields of view per
849 group, respectively. Data are presented as mean ± SEM.

850 (F) Representative TEM images of membrane structures reconstituted with *Atg7*
851 knockout membranes (protocol A). Conditions: I, reconstitution buffer containing 40
852 μg/mL digitonin; II: buffer (reconstitution buffer containing 40 μg/mL digitonin)
853 supplemented with *Atg7* knockout S150, ATP, and GTP; III: buffer supplemented with
854 WT S150, ATP, and GTP. Red arrows indicate autolamellasomes. Boxed regions are
855 magnified and demonstrated on the right. Scale bar, 500 nm.

856 (G) Western blot analysis of extracted S150 from WT and *Atg7* knockout NRK cells.

857 (H) Quantification of sealed mature autollamellasomes (Mature) and unsealed
858 autollamellasome precursors from the *in vitro* reconstitution system in (F). More than
859 45 fields of view were analyzed per group. Data are presented as mean ± SEM.

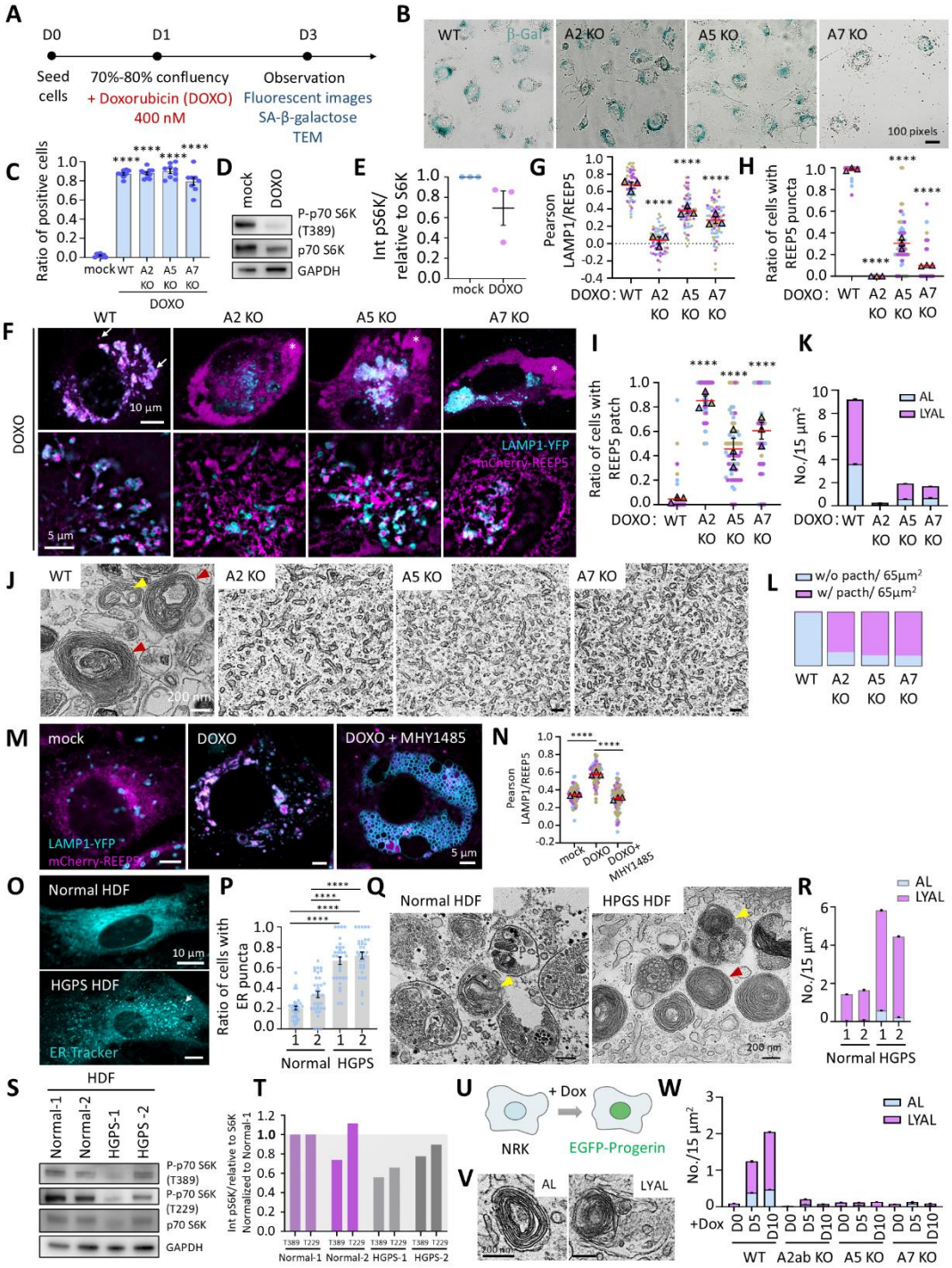

Figure 7 Autolamellasomes increased in senescent cells and progeroid cells.

(A) Schematic diagram illustrating the process of Doxorubicin-induced cellular senescence.

(B) β-galactosidase staining results of WT and autophagy-deficient NRK cells. Scale bar, 100 pixels.

(C) Quantification of β-galactosidase-positive cell ratios from (B). More than 45 cells were analyzed per group. Data are presented as mean ± SEM. ****, $p<0.0001$. P values were calculated using a two-tailed, unpaired t test.

(D) Western blot results of NRK cells treated with or without 400 nM Doxorubicin (DOXO) for 2 days. Cell lysates were subjected to SDS-PAGE and immunoblotted with the indicated antibodies. GAPDH served as a loading control. Blots are representative of n=3 independent biological replicates.

(E) Quantification of phospho-p70 S6K (T389) band intensities from (D). Individual data points represent values normalized to total p70 S6K and expressed relative to the untreated control. n=3 independent biological repeats. Data are presented as mean ± SEM.

(F) Representative confocal (upper layer) and SIM images (lower layer) of Doxorubicin (DOXO)-treated WT and autophagy-deficient NRK cells. Arrows indicate ER puncta; asterisks indicate ER patches. Scale bars: 10 μm (confocal), 5 μm (SIM).

(G-I) Statistics of cells from (F). (G) Pearson correlation coefficient of LAMP1 and REEP5 signals. (H) Ratio of cells with ER puncta. (I) Ratio of cells with ER patches. More than 49 cells were analyzed in each group for each experiment (n=3 independent biological repeats). Data are presented as mean ± SEM. ****, $p<0.0001$. P values were calculated using a two-tailed, unpaired t test.

(J) Representative TEM images of Doxorubicin (DOXO)-treated WT and autophagy-deficient NRK cells. Red arrows indicate autolamellasomes (AL), yellow arrow indicates lysosomes containing with autolamellasomes (LYAL). Scale bar, 200 nm.

(K) TEM images from (J) were quantified for the amount of each kind of structure (AL: autolamellasome, LYAL: lysosome/autolysosome containing with autolamellasome) in 15 μm^2 area. More than 39 cells were imaged for each group. Data are reported as mean ± SEM.

(L) Quantification of frequency of existence of ER patch per 65 μm^2 area from TEM images in (J).

(M) Representative confocal images of NRK cells treated with or without 400 nM

895 Doxorubicin (DOXO), 400 nM DOXO together with 10 μM MHY1485 for 2 days.
896 Scale bars, 5 μm.
897 (N) Quantification of the Pearson correlation coefficient of LAMP1 and REEP5 signals
898 from (M). More than 130 cells were analyzed in each group for each experiment (n=3
899 independent biological repeats). Data are presented as mean ± SEM. ****, $p<0.0001$.
900 P values were calculated using a two-tailed, unpaired t test.
901 (O) Representative confocal images of ER Tracker-labeled HDF (human dermal
902 fibroblasts) from normal donors and HGPS (Hutchinson-Gilford progeria syndrome)
903 patients. Scale bars, 10 μm.
904 (P) Quantification of the ratio of cells with ER puncta from (O). Normal HDF from 2
905 healthy donors and HGPS HDF form 2 HGPS patients were acquired. More than 225
906 cells were analyzed for each group. Data are reported as mean ± SEM. ****, $p<0.0001$.
907 P values were calculated using a two-tailed, unpaired t test.
908 (Q) Representative TEM images of Normal HDF and HGPS HDF. Red arrow indicates
909 autolamellasome (AL), yellow arrows indicate lysosome/autolysosome containing with
910 autolamellasomes (LYAL). Scale bars, 200 nm.
911 (R) TEM images from (Q) were quantified for the amount of each kind of structure (AL:
912 autolamellasome, LYAL: lysosome/autolysosome containing with autolamellasome) in
913 15 μm^2 area. More than 65 areas were imaged for each group. Data are reported as mean
914 ± SEM.
915 (S) Western blot results of indicated HDF. Cell lysates were subjected to SDS-PAGE
916 and immunoblotted with the indicated antibodies. GAPDH served as a loading control.
917 (T) Phospho-p70 S6K (T389) and phospho-p70 S6K (T229) band intensities from (S)
918 were normalized to total p70 S6K and expressed relative to Normal-1.
919 (U) Schematic diagram illustrating doxycycline (Dox) inducible expression of EGFP-
920 Progerin in NRK cells.
921 (V) Representative TEM images of AL (autolamellasome) and LYAL
922 (lysosome/autolysosome containing with autolamellasome) in doxycycline (Dox)-
923 induced EGFP-Progerin NRK cells. Scale bars, 200 nm.

924 (W) Quantification of AL (autolamellasome) and LYAL (lysosome/autolysosome
925 containing autolamellasomes) number per 15 μm^2 area from TEM images from (V).
926 WT and autophagy-deficient NRK cells were treated with doxycycline (Dox) for 0, 5,
927 and 10 days (D0, D5, D10). More than 60 areas were imaged for each group. Data are
928 reported as mean ± SEM.
929

930 **Extended figures and figure legends**

931

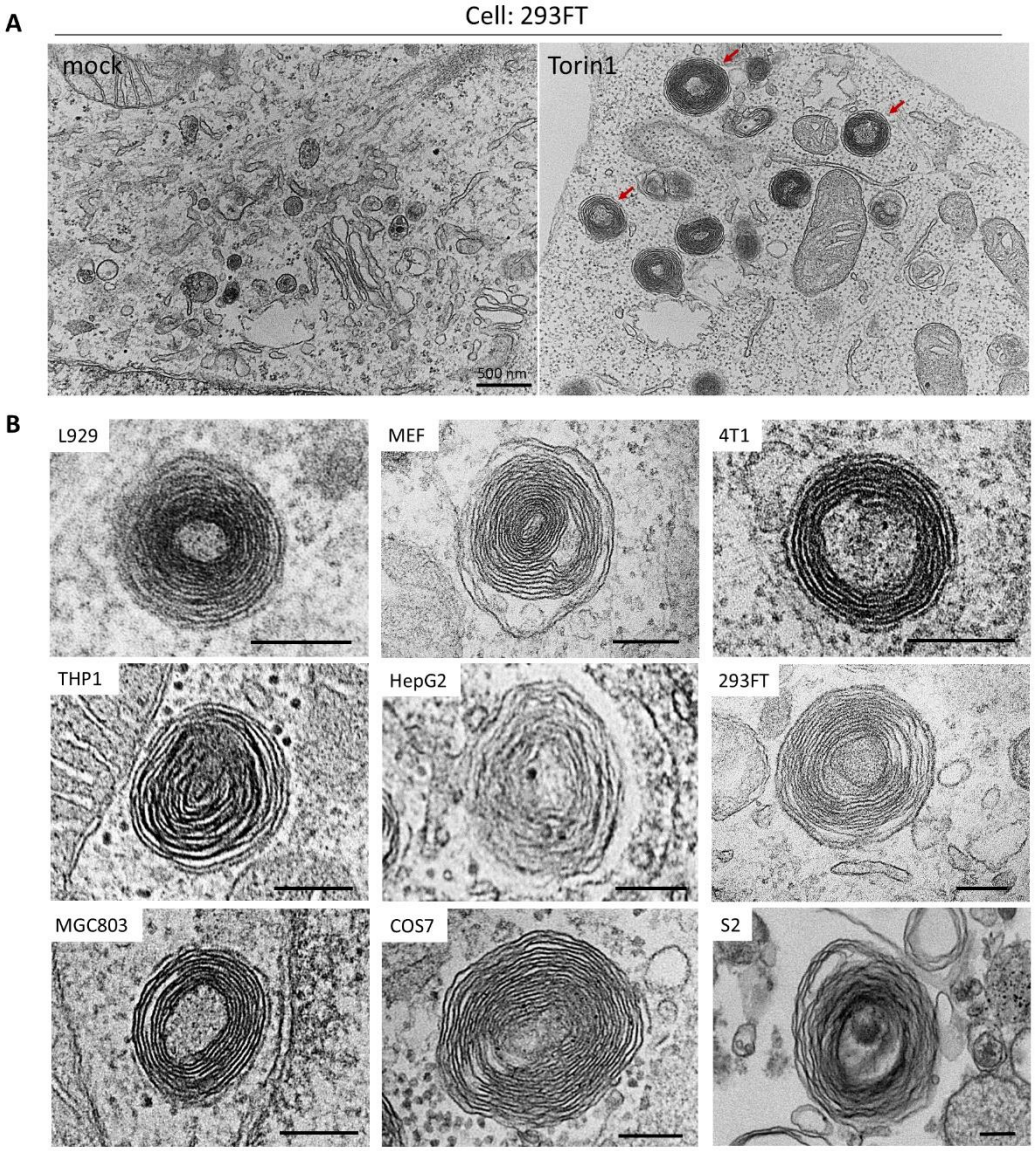

932

933 **Extended Data Fig. 1. Free whorl formation is a widespread phenomenon.**

934 (A) Representative TEM images of 293FT cells treated with or without 1 μM Torin1

935 for 24 h. Scale bar, 500 nm.

936 (B) Representative TEM images of free whorls in various cells treated with 1 μM

937 Torin1 for 24 h. Scale bars, 200 nm.

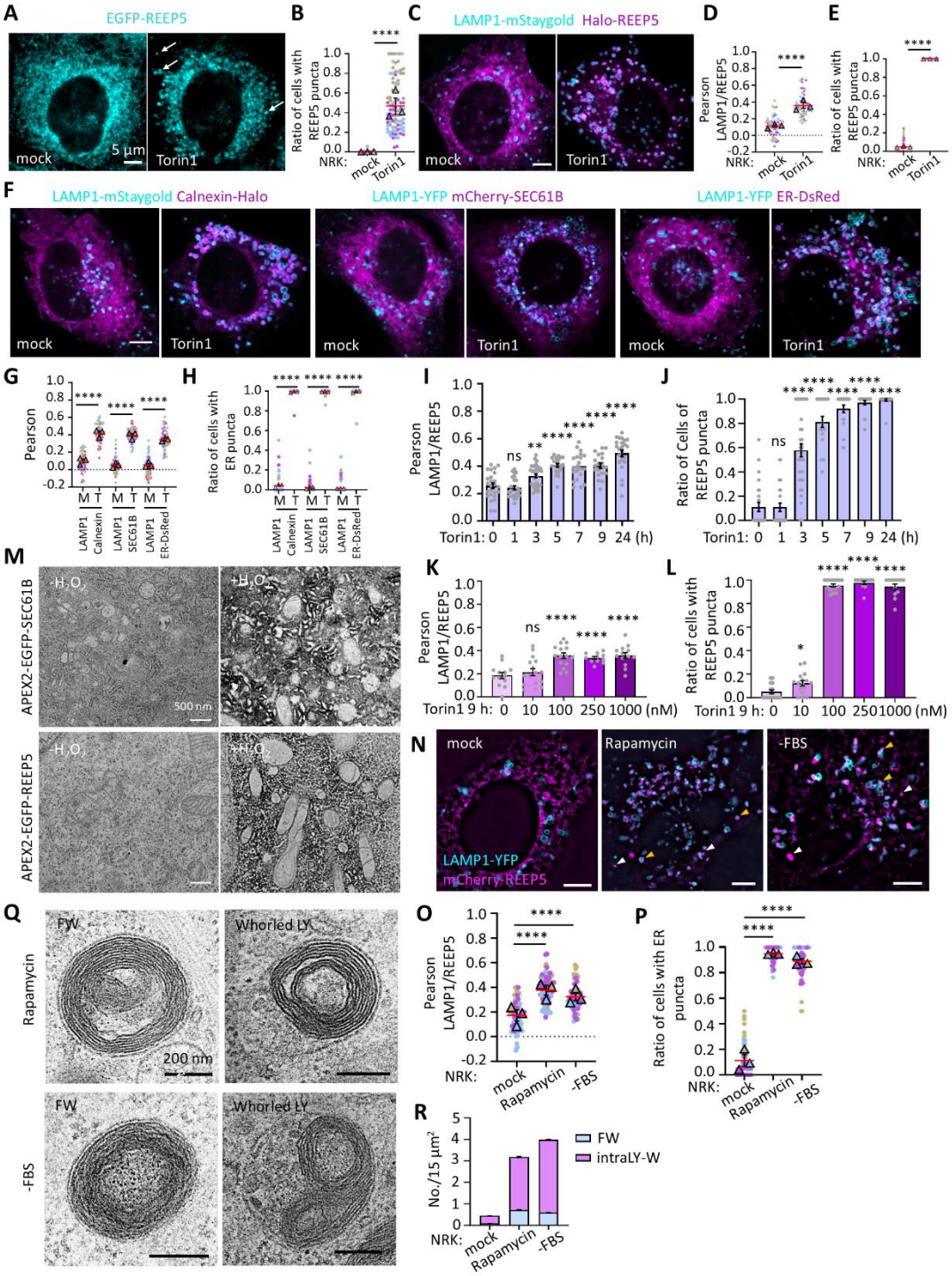

938

939 **Extended Data Fig. 2. Whorls originate from the endoplasmic reticulum.**

940 (A) Representative confocal images of NRK cells stably expressing EGFP-REEP5

941 treated with or without 1 μM Torin1 for 24 h. Arrows indicate EGFP-REEP5 labeled-

942 ER puncta. Scale bar, 5 μm.

943 (B) Quantification of the ratio of cells shown in (A) contained with ER puncta. More

944 than 280 cells were analyzed per group in each experiment (n=3 experiments). Error
945 bars indicate mean ± SEM. ****, p<0.0001. P values were calculated using a two-tailed,
946 unpaired t test.
947 (C) Representative confocal images of NRK cells stably expressing LAMP1-
948 mStaygold/HaloTag-REEP5 treated with or without 1 μM Torin1 for 24 h. Scale bar, 5
949 μm.
950 (D-E) Quantification of the cells shown in (C). (D) Pearson correlation coefficient of
951 LAMP1-mStaygold and HaloTag-REEP5 signals. (E) Ratio of cells with HaloTag-
952 REEP5 labeled-ER puncta. More than 280 cells were analyzed per group in each
953 experiment (n=3 experiments). Error bars indicate mean ± SEM. ****, p<0.0001. P
954 values were calculated using a two-tailed, unpaired t test.
955 (F) Representative confocal images of NRK cells stably expressing LAMP1-
956 mStaygold/Calnexin-HaloTag, LAMP1-YFP/mCherry-SEC61B, LAMP1-YFP/ER-
957 DsRed treated with or without 1 μM Torin1 for 24 h. Scale bar, 5 μm.
958 (G-H) Quantification of the cells shown in (F). (G) Pearson correlation coefficient of
959 LAMP1 and ER proteins. (H) Ratio of cells with ER puncta. Sample sizes (n) were
960 n>90 (Calnexin), n>100 (SEC61B), and n>50 (ER-DsRed) cells per group in each
961 experiment (n=3 experiments). Error bars indicate mean ± SEM. ****, p<0.0001. P
962 values were calculated using a two-tailed, unpaired t test.
963 (I-J) Quantification of NRK cells stably co-expressing LAMP1-YFP and mCherry-
964 REEP5 treated with 1 μM Torin1 in a time series. (I) Pearson correlation coefficient of
965 LAMP1 and REEP5 signals. (J) Ratio of cells with ER puncta. More than 85 cells were
966 analyzed in each time point. Error bars indicate mean ± SEM. ns, not significant, **,
967 p<0.01, ****, p<0.0001. P values were calculated using a two-tailed, unpaired t test.
968 (K-L) NRK cells stably expressing LAMP1-YFP and mCherry-REEP5 were treated
969 with Torin1 at the indicated concentrations for 9 h. (K) Pearson correlation coefficient
970 of LAMP1 and REEP5 signals. (L) Ratio of cells exhibiting ER puncta. More than 160
971 cells were analyzed per dose. Data are presented as mean ± SEM. ns, not significant, *,
972 p<0.05, ****, p<0.0001. P values were calculated using a two-tailed, unpaired t test.

973 (M) APEX2-TEM images of cells stably expressing APEX2-EGFP-SEC61B or
974 APEX2-EGFP-REEP5. In H_2O_2-treated groups, APEX2 catalyzes DAB polymerization,
975 generating electron-dense structures that reveal protein localization. In the absence of
976 H_2O_2, cells exhibit low electron contrast. Scale bars, 500 nm.
977 (N) Representative SIM images of NRK cells stably co-expressing LAMP1-
978 YFP/mCherry-REEP5. Cells were treated with 1 μM rapamycin or serum-starved (FBS
979 withdrawal) for 24 h, alongside untreated controls. White arrows: free-standing ER
980 puncta, yellow arrows: ER puncta inside lysosomes. Scale bars, 5 μm.
981 (O-P) Quantification of the cells shown in (N). (O) Pearson correlation coefficient of
982 LAMP1 and REEP5 signals. (P) Ratio of cells with ER puncta. More than 180 cells
983 were analyzed in each group. Error bars indicate mean ± SEM. ****, $p<0.0001$. P
984 values were calculated using a two-tailed, unpaired t test.
985 (Q) Representative TEM images of free whorls (FW) and intralysosomal whorls
986 (intraLY-W) in NRK cells treated with 1 μM rapamycin or serum-starved (FBS
987 withdrawal) for 24 h. Scale bar, 200 nm.
988 (R) TEM images from (Q) were quantified for the amount of each kind of structure
989 (FW: free whorls, intraLY-W: intralysosomal whorls) in 15 μm^2 area. More than 70
990 cells were imaged for each group. Data are reported as mean ± SEM.
991

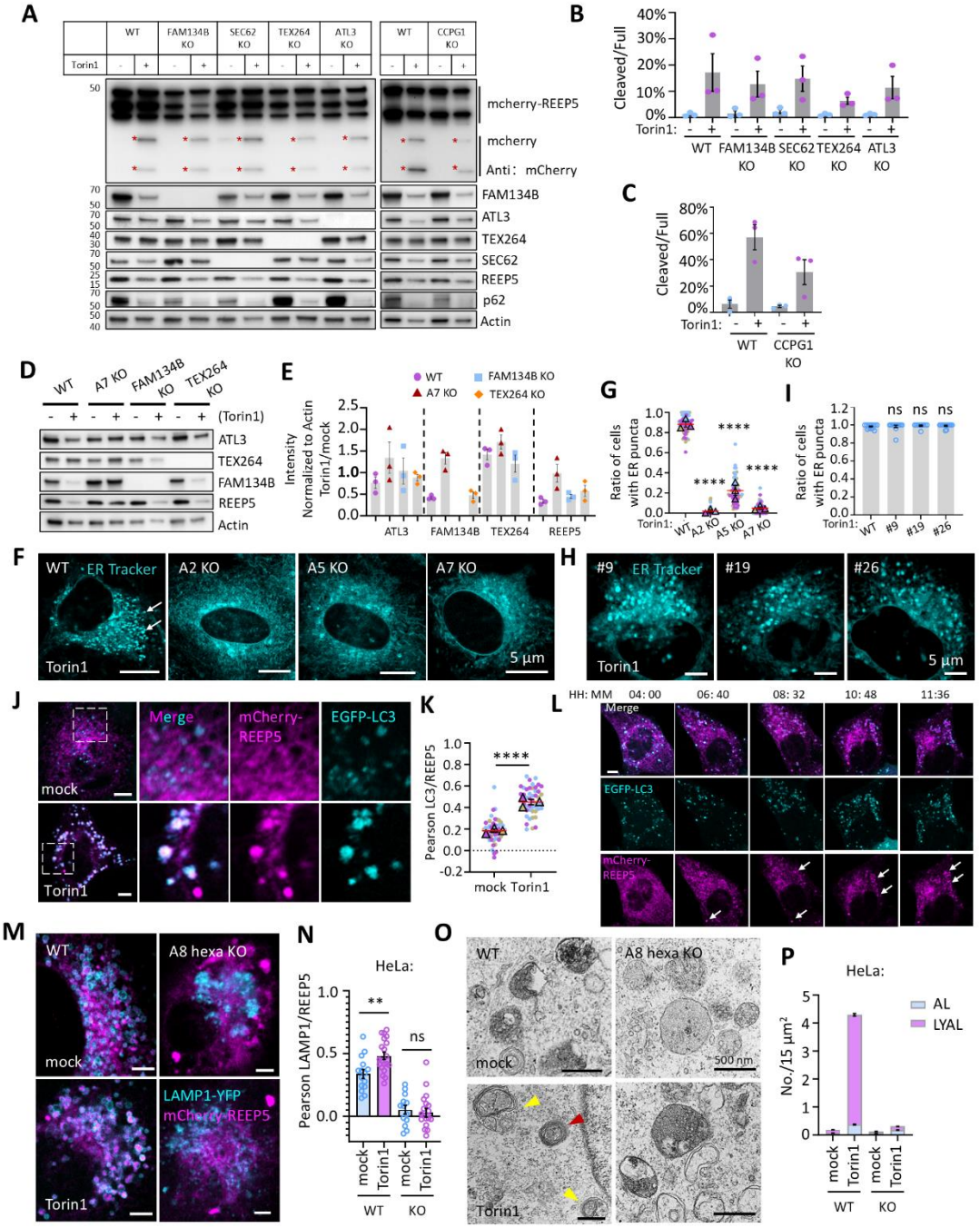
A
WT
FAM134B KO
SEC62 KO
TEX264 KO
ATL3 KO
CCPG1 KO
Torin1
mcherry-REEP5
mcherry
Anti：mCherry
FAM134B
ATL3
TEX264
SEC62
REEP5
p62
Actin
B
Cleaved/Full
Torin1:
WT
FAM134B KO
SEC62 KO
TEX264 KO
ATL3 KO
C
Cleaved/Full
Torin1:
WT
CCPG1 KO
D
WT
A7 KO
FAM134B KO
TEX264 KO
(Torin1)
ATL3
TEX264
FAM134B
REEP5
Actin
E
WT
A7 KO
FAM134B KO
TEX264 KO
Intensity Normalized to Actin
Torin1/mock
ATL3
FAM134B
TEX264
REEP5
G
Ratio of cells with ER puncta
Torin1:
WT
A2 KO
A5 KO
A7 KO
I
Ratio of cells with ER puncta
Torin1:
WT
#9
#19
#26
ns
F
WT
ER Tracker
A2 KO
A5 KO
A7 KO
Torin1
5 μm
H
#9
ER Tracker
#19
#26
Torin1
5 μm
J
Merge
mCherry-REEP5
EGFP-LC3
mock
Torin1
K
Pearson LC3/REEP5
mock
Torin1
L
HH: MM
04: 00
06: 40
08: 32
10: 48
11:36
Merge
EGFP-LC3
mCherry-REEP5
M
WT
A8 hexa KO
mock
Torin1
LAMP1-YFP
mCherry-REEP5
N
HeLa:
Pearson LAMP1/REEP5
mock
Torin1
WT
KO
O
WT
A8 hexa KO
mock
500 nm
Torin1
P
HeLa:
AL
LYAL
No./15 μm²
mock
Torin1
WT
KO

992

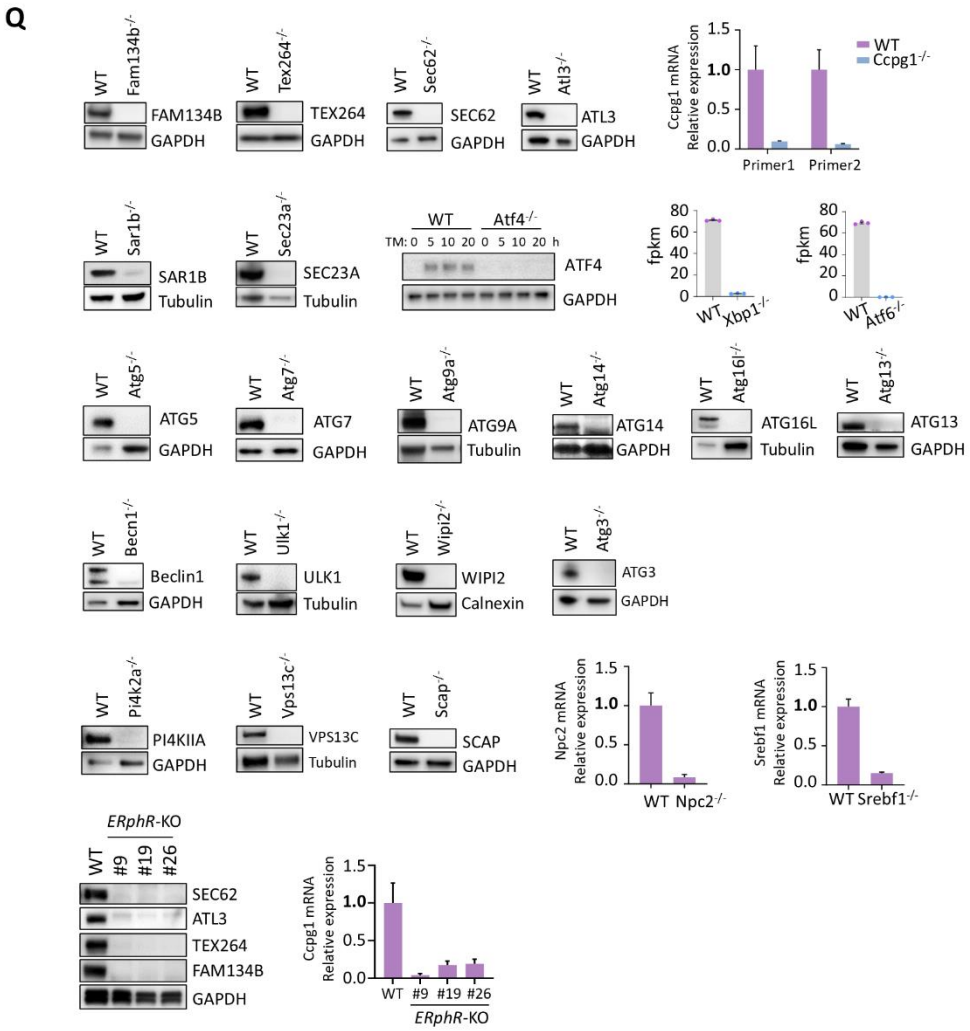

Extended Data Fig. 3. Autolamellasome formation depends on autophagy core machinery but not ER phagy receptors.

(A) Western blot analysis of endogenous proteins and mCherry cleavage in WT and ER phagy receptor KO NRK cells. WT, *Fam134b* KO, *Sec62* KO, *Tex264* KO, *Atl3* KO and *Ccpg1* KO NRK cells were treated with or without 1 μM Torin1 for 24 h. Cell lysates were subjected to SDS-PAGE and immunoblotted with the indicated antibodies. Asterisks denote cleaved mCherry fragments generated upon autophagic degradation. Actin served as a loading control. Blots are representative of n=3 independent biological replicates.

(B-C) Quantification of mCherry-REEP5 cleavage. The percentage of cleaved mCherry fragments relative to full-length mCherry-REEP5 was quantified from the Western blot

1005 shown in (A). Data are presented as mean ± SEM from n=3 independent biological
1006 replicates.
1007 (D) Western blot analysis of endogenous proteins in WT, *Atg7* KO, *Fam134b* KO and
1008 *Tex264* KO NRK cells treated with or without 1 μM Torin1 for 24 h. Cell lysates were
1009 subjected to SDS-PAGE and immunoblotted with the indicated antibodies. Actin
1010 served as a loading control. Blots are representative of n=3 independent biological
1011 replicates.
1012 (E) Quantification of integrated band intensities from (D). Individual data points
1013 represent relative protein levels in the Torin1-treated group normalized to the untreated
1014 control and loading control Actin. n=3 independent biological repeats. Data are
1015 presented as mean ± SEM.
1016 (F) Representative confocal images of WT and autophagy-deficient KO (*Atg2* KO, *Atg5*
1017 KO, *Atg7* KO) NRK cells treated with 1 μM Torin1 for 24 h. NRK cells were labeled
1018 by ER Tracker. Arrows indicate ER puncta. Scale bars, 5 μm.
1019 (G) Quantification of the ratio of cells shown in (F) contained with ER puncta. More
1020 than 250 cells were analyzed per group in each experiment (n=3 experiments). Error
1021 bars indicate mean ± SEM. ****, $p<0.0001$. P values were calculated using a two-tailed,
1022 unpaired t test.
1023 (H) Representative confocal images of *ERphR* KO NRK cells treated with 1 μM Torin1
1024 for 24 h. NRK cells are labeled by ER Tracker. Arrows indicate ER puncta. Scale bars,
1025 5 μm.
1026 (I) Quantification of the ratio of cells shown in (H) contained with ER puncta. More
1027 than 89 cells were analyzed per group. Error bars indicate mean ± SEM. ns, not
1028 significant. P values were calculated using a two-tailed, unpaired t test.
1029 (J) Representative confocal images of NRK cells stably co-expressing EGFP-LC3 and
1030 mCherry-REEP5 treated with or without 1 μM Torin1 for 24 h. Scale bars, 5 μm.
1031 (K) Pearson correlation coefficient of LC3 and REEP5 signals of the cells shown in (J).
1032 More than 100 cells were analyzed for each group in each experiment (n=3 independent
1033 experiments). Error bars indicate mean ± SEM. ****, $p<0.0001$. P values were

1034 calculated using a two-tailed, unpaired t test.

1035 (L) Time-lapse live cell images of NRK cells stably co-expressing EGFP-LC3 and
1036 mCherry-REEP5 treated with Torin1. Here shows representative snapshots at indicated
1037 time points. Scale bar, 5 μm.

1038 (M) WT and *Atg8* hexa KO HeLa cells stably co-expressing LAMP1-YFP and
1039 mCherry-REEP5 were treated with or without 1 μM Torin1 for 24 h. More than 30 cells
1040 were analyzed for each group. Scale bars, 5 μm.

1041 (N) Pearson correlation coefficient of LAMP1 and REEP5 signals of the cells shown in
1042 (M). More than 30 cells were analyzed for each group. Error bars indicate mean ± SEM.
1043 **, $p<0.01$, ns, not significant. P values were calculated using a two-tailed, unpaired t
1044 test.

1045 (O) Representative TEM images of WT and *Atg8* hexa KO HeLa cells treated with or
1046 without 1 μM Torin1 for 24 h. Red arrow indicates autolamellasome (AL), yellow
1047 arrows indicate lysosome/autolysosome containing with autolamellasomes (LYAL).
1048 Scale bars, 500 nm.

1049 (P) TEM images from (O) were quantified for the amount of each kind of structure (AL:
1050 autolamellasome, LYAL: lysosome/autolysosome containing with autolamellasome) in
1051 15 μm^2 area. More than 45 cells were imaged for each group. Data are reported as mean
1052 ± SEM.

1053 (Q) Verification of knockout cells. Western blot results, quantitative RT-PCR and fpkm
1054 values are shown here.

1055

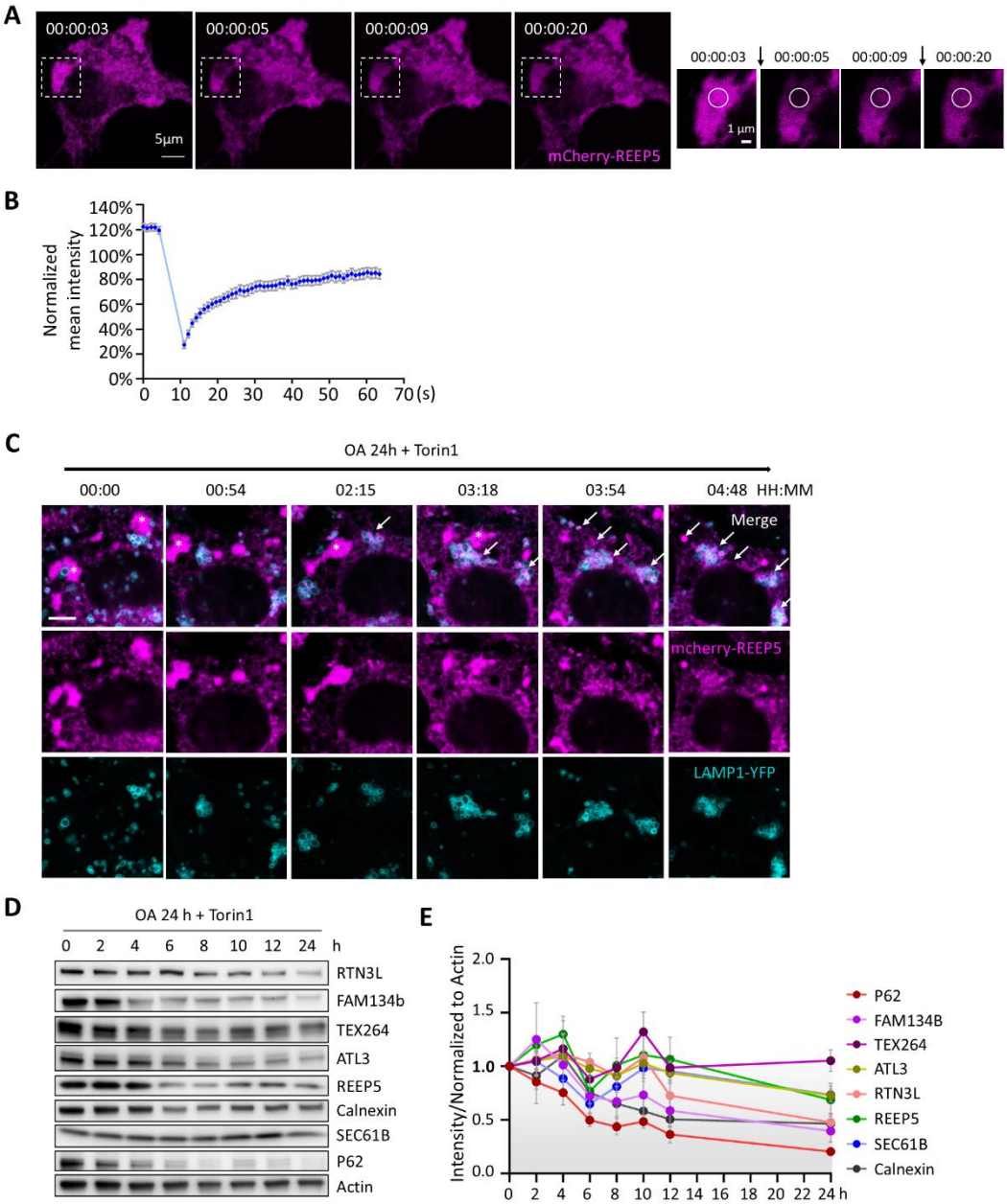

Extended Data Fig. 4. Autophagy-dependent assembly of autolamellasome from ER fragments.

(A) FRAP analysis of OAT-treated NRK-*Atg7*-KO cells stably expressing mCherry-REEP5. The boxed regions are magnified on the right. Dashed circles indicate the bleached region. Time intervals are indicated relative to bleaching. Scale bars: 5 μm (main image) and 1 μm (magnified view).

(B) Normalized mean fluorescence intensity of the bleached region over time. More

1064 than 20 cells were analyzed. Data are presented as mean ± SEM. Intensity values were
1065 normalized to pre-bleach levels.
1066 (C) Time-lapse live cell images of NRK cells stably co-expressing LAMP1-YFP and
1067 mCherry-REEP5 treated with OAT. Here shows representative snapshots at indicated
1068 time points. Arrows indicate ER puncta while asterisks indicate ER patches. Scale bar,
1069 5 μm.
1070 (D) Western blot results of NRK cells treated with 200 μM OA 24 h followed by 1 μM
1071 Torin1 in a time series. Cell lysates were subjected to SDS-PAGE and immunoblotted
1072 with the indicated antibodies. Blots are representative of n=3 independent biological
1073 replicates.
1074 (E) Quantification of integrated band intensities from (D). Individual data points
1075 represent relative protein levels in the time point normalized to 0 h and loading control
1076 Actin. n=3 independent biological repeats. Data are presented as mean ± SEM.

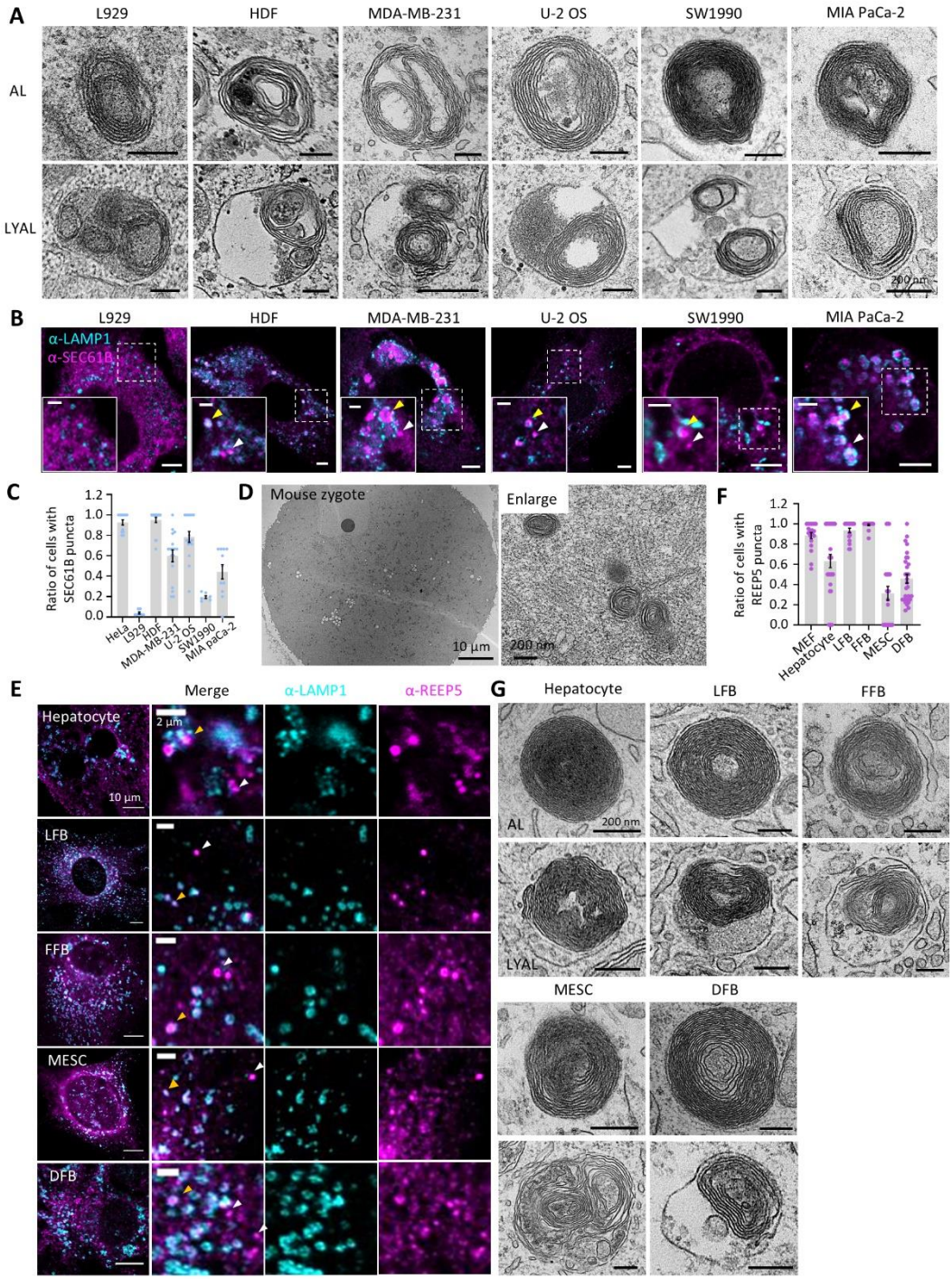

Extended Data Fig. 5. Basal formation of autolamellasomes in cell lines and primary cells.

(A) Representative TEM images of AL (autolamellasome) and LYAL (lysosome/autolysosome containing with autolamellasome) in indicated cell lines. Scale bars, 200 nm.

1083 (B) Indicated cell lines were co-stained with anti-LAMP1 and anti-SEC61B antibodies.
1084 White arrows: free-standing ER puncta, yellow arrows: ER puncta inside lysosomes.
1085 Scale bars: 5 μm (main image) and 2 μm (magnified view).
1086 (C) Statistic of cells from (B) for the ratio of cells with SEC61B puncta. More than 38
1087 cells were analyzed for each group. Data are presented as mean ± SEM.
1088 (D) Representative TEM images of whole mouse zygote (scale bar=10 μm) and
1089 enlarged view (scale bar=200 nm).
1090 (E) Indicated primary cells were co-stained with anti-LAMP1 and anti-REEP5
1091 antibodies. White arrows: free-standing ER puncta, yellow arrows: ER puncta inside
1092 lysosomes. Scale bars: 10 μm (main image) and 2 μm (magnified view).
1093 (F) Statistic of cells from (E) for the ratio of cells with REEP5 puncta. More than 60
1094 cells were analyzed for each group. Data are presented as mean ± SEM.
1095 (G) Representative TEM images of AL (autolamellasome) and LYAL
1096 (lysosome/autolysosome containing with autolamellasome) in indicated primary cells.
1097 Scale bars, 200 nm.

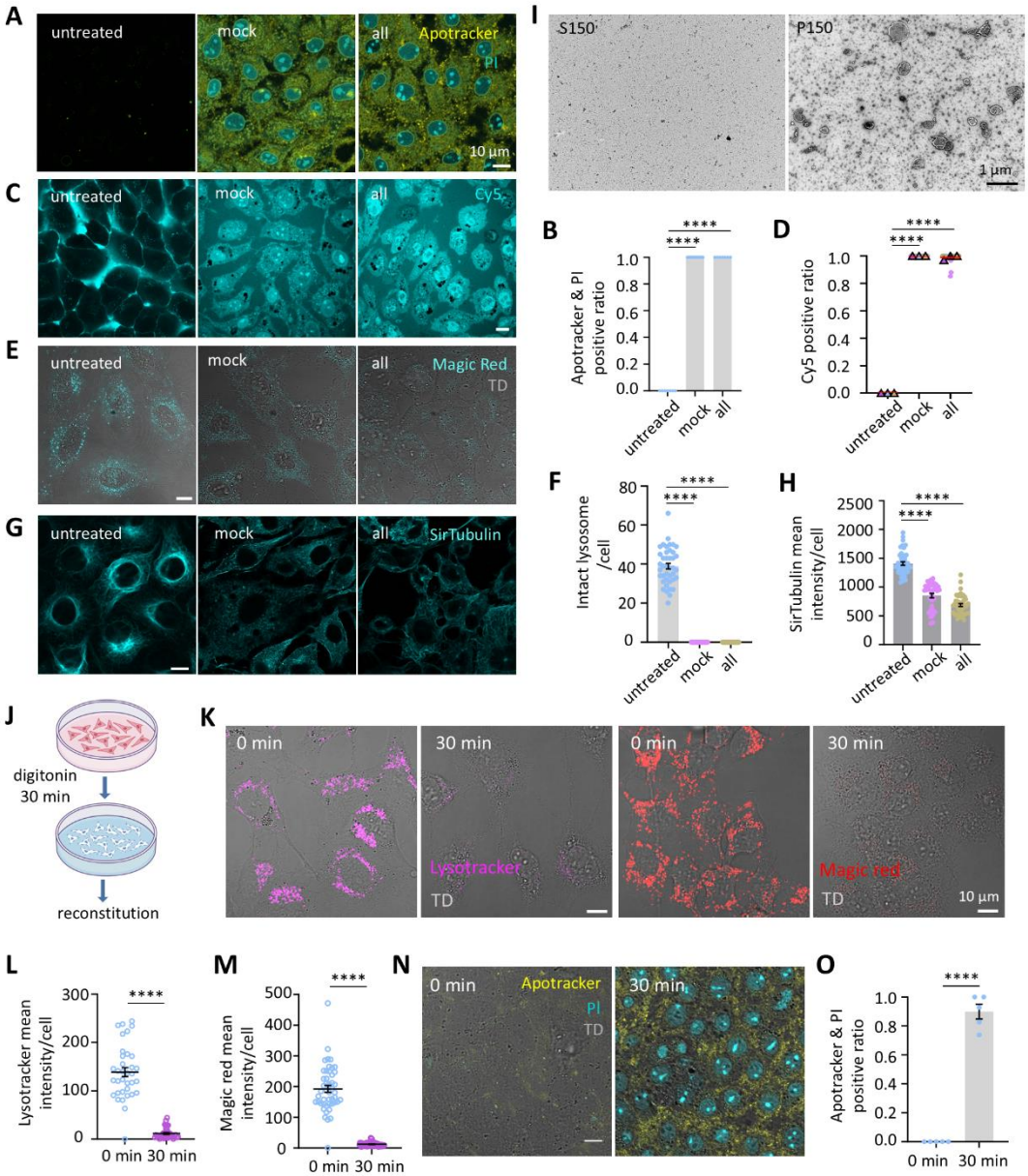

Extended Data Fig. 6. *In vitro* reconstitution of autolamellasome.

(A) Representative confocal images of cells following protocol A. Cell death was verified using Apotracker and propidium iodide (PI). Scale bar, 10 μm.

(B) Quantification of the ratio of cells double-positive for Apotracker and PI from (A). More than 150 cells were analyzed per group. Data are presented as mean ± SEM. ****, $p<0.0001$. P values were calculated using a two-tailed, unpaired t test.

(C) Representative confocal images of cells following protocol A. Cell permeability was verified using Cy5. Scale bar, 10 μm.

1107 (D) Quantification of the ratio of Cy5-positive cells in (C). More than 85 cells were
1108 analyzed per group in each experiment (n=3 independent biological repeats). Data are
1109 presented as mean ± SEM. ****, p<0.0001. P values were calculated using a two-tailed,
1110 unpaired t test.
1111 (E) Representative confocal images of cells following protocol A. Lysosome integrity
1112 was verified using Magic Red. Scale bar, 10 μm.
1113 (F) Quantification of intact lysosomes per cell from (E). More than 40 cells were
1114 analyzed per group. Data are presented as mean ± SEM. ****, p<0.0001. P values were
1115 calculated using a two-tailed, unpaired t test.
1116 (G) Representative confocal images of cells following protocol A. Microtubule
1117 integrity was verified using SirTubulin. Scale bar, 10 μm.
1118 (H) Quantification of microtubule mean intensity per cell in (G). More than 37 cells
1119 were analyzed per group. Data are presented as mean ± SEM. ****, p<0.0001. P values
1120 were calculated using a two-tailed, unpaired t test.
1121 (I) Negative staining-TEM images of S150 and P150. Scale bar, 1 μm.
1122 (J) Schematic diagram illustrating the process of *in vitro* reconstitution (Protocol D).
1123 OA primmed NRK cells were permeabilized in reconstitution buffer containing 40
1124 μg/mL digitonin for 30 min, followed by incubation in reconstitution buffer (mock
1125 group) or buffer supplemented with S150, ATP and GTP (all group) for 6-8 h at 30 ℃.
1126 (K) Representative confocal images of cells following protocol D. NRK cells were
1127 treated with or without 40 μg/mL digitonin for 30 min. Lysosome integrity was verified
1128 using Lysotracker and Magic Red. Scale bars, 10 μm.
1129 (L-M) Quantification of mean intensity of Lysotracker signals (L) or Magic Red signals
1130 (M) from cells in (K). More than 34 cells were analyzed per group for (L) and more
1131 than 45 cells were analyzed per group for (M). Data are presented as mean ± SEM.
1132 ****, p<0.0001. P values were calculated using a two-tailed, unpaired t test.
1133 (N) Cell death in NRK cells following protocol D were verified using Apotracker and
1134 PI staining and imaged by confocal microscope. Scale bar, 10 μm.
1135 (O) Quantification of the ratio of cells positive for both Apotracker and PI from (N).

1136 More than 100 cells were analyzed per group. Data are presented as mean ± SEM. ****,

1137 $p<0.0001$. P values were calculated using a two-tailed, unpaired t test.

1138

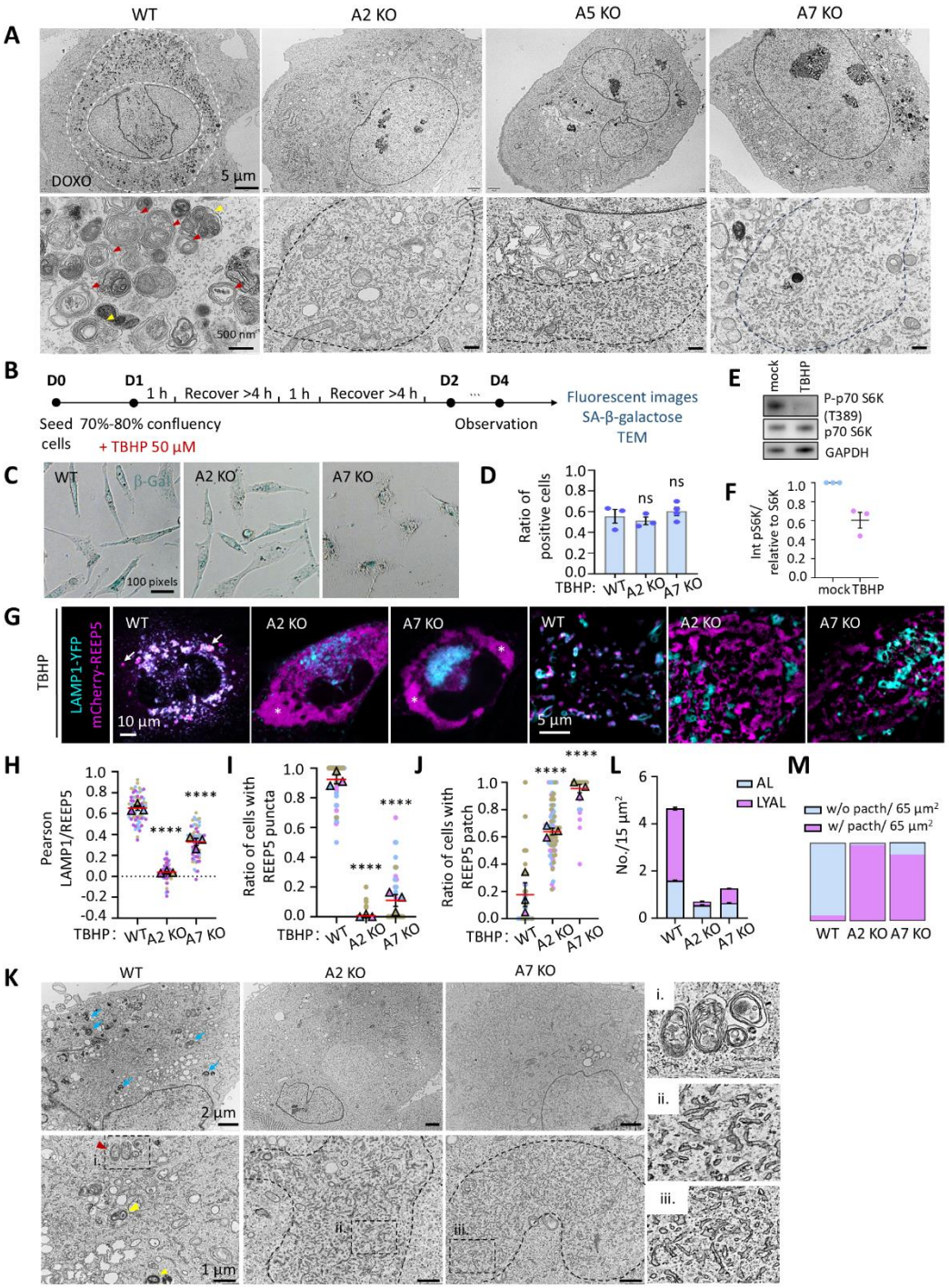
A
WT
A2 KO
A5 KO
A7 KO
DOXO
5 µm
500 nm
B
D0
D1
1 h
Recover >4 h
1 h
Recover >4 h
D2
D4
Seed cells
70%-80% confluency
+ TBHP 50 µM
Observation
Fluorescent images
SA-β-galactose
TEM
C
β-Gal
100 pixels
D
Ratio of positive cells
ns
ns
TBHP: WT A2 KO A7 KO
E
mock
TBHP
P-p70 S6K (T389)
p70 S6K
GAPDH
F
Int pS6K/ relative to S6K
mock TBHP
G
TBHP
LAMP1-YFP
mCherry-REEP5
10 µm
5 µm
H
Pearson LAMP1/REEP5
****
****
TBHP: WT A2 KO A7 KO
I
Ratio of cells with REEP5 puncta
****
****
TBHP: WT A2 KO A7 KO
J
Ratio of cells with REEP5 patch
****
****
TBHP: WT A2 KO A7 KO
L
No./15 µm²
AL
LYAL
WT A2 KO A7 KO
M
w/o pacth/ 65 µm²
w/ pacth/ 65 µm²
WT A2 KO A7 KO
K
WT
A2 KO
A7 KO
2 µm
1 µm
i.
ii.
iii.

1139

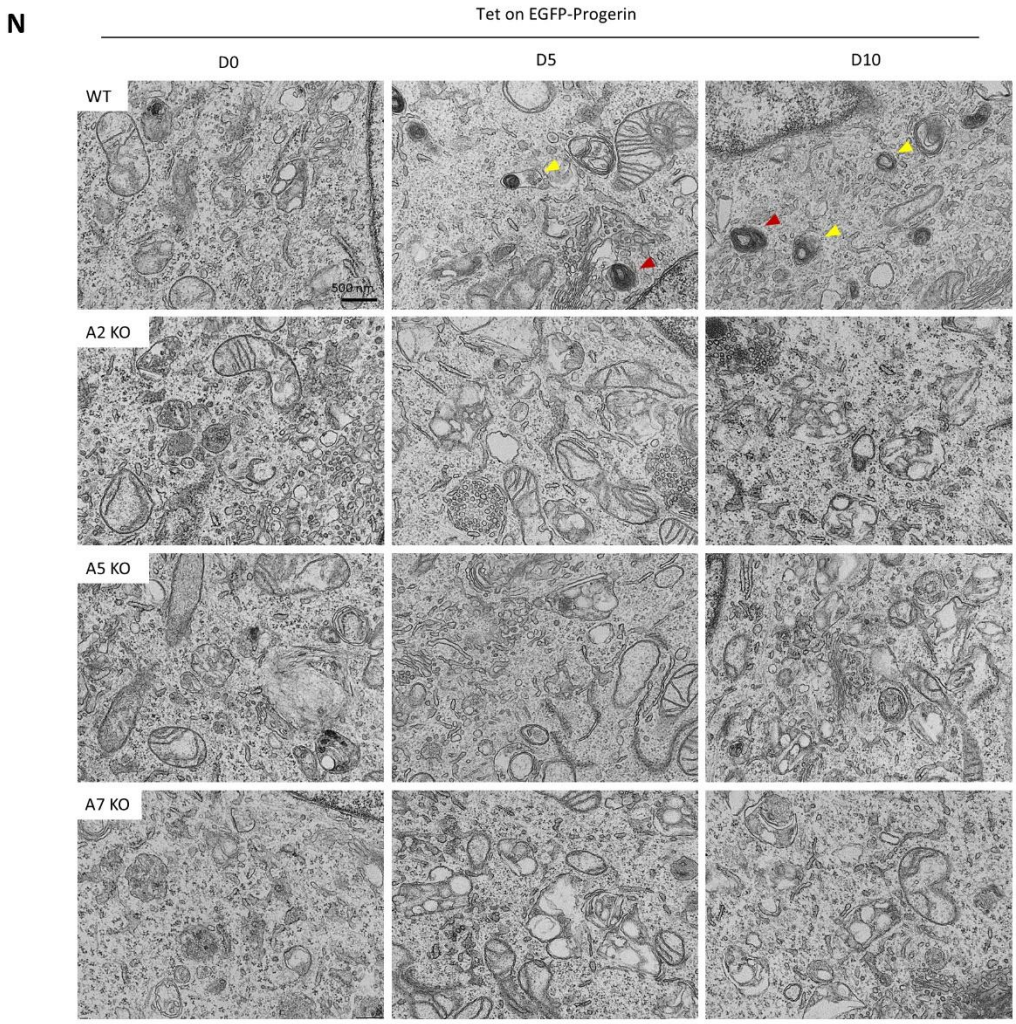

Extended Data Fig. 7. Increased basal autolamellasome formation in senescent cells and cells from premature aging patients.

(A) Representative TEM images of DOXO-induced senescent WT and autophagy-deficient NRK cells. White dashed lines indicate accumulation of whorls. Black dashed lines indicate clusters of ER fragments. Red arrows indicate autolamellasomes (AL) and yellow arrows indicate lysosome/autolysosome containing with autolamellasome (LYAL). Scale bars: 5 μm (large view), 500 nm (magnified view).

(B) Schematic diagram illustrating the process of TBHP-induced cellular senescence.

(C) β-galactosidase staining results of WT and autophagy-deficient (*Atg2* KO and *Atg7* KO) NRK cells after TBHP treatment. *Atg5* KO NRK cells died shortly after treatment. Scale bar, 100 pixels.

(D) Quantification of β-galactosidase-positive cell ratios from (C). More than 40 cells

1153 were analyzed per group. Data are presented as mean ± SEM. ns, not significant. P
1154 values were calculated using a two-tailed, unpaired t test.
1155 (E) Western blot results of NRK cells treated with or without TBHP as indicated in (B).
1156 Cell lysates were subjected to SDS-PAGE and immunoblotted with the indicated
1157 antibodies. GAPDH served as a loading control. Blots are representative of n=3
1158 independent biological replicates.
1159 (F) Quantification of phospho-p70 S6K (T389) band intensities from (E). Individual
1160 data points represent values normalized to total p70 S6K and expressed relative to the
1161 untreated control. n=3 independent biological repeats. Data are presented as mean ±
1162 SEM.
1163 (G) Representative confocal (left layer) and SIM images (right layer) of TBHP-treated
1164 WT and autophagy-deficient NRK cells. Arrows indicate ER puncta; asterisks indicate
1165 ER patches. Scale bars denote 10 μm for confocal images and 5 μm for SIM images.
1166 (H-J) Statistics of cells from (G). (H) Pearson correlation coefficient of LAMP1 and
1167 REEP5 signals. (I) Ratio of cells with ER puncta. (J) Ratio of cells with ER patches.
1168 More than 65 cells were analyzed in each group for each experiment (n=3 independent
1169 biological repeats). Data are presented as mean ± SEM. ****, $p<0.0001$. P values were
1170 calculated using a two-tailed, unpaired t test.
1171 (K) Representative TEM images of TBHP-treated WT and autophagy-deficient NRK
1172 cells. Blue arrows indicate electron dense structures, red arrows indicate
1173 autolamellasome (AL), and yellow arrow indicates lysosome/autolysosome containing
1174 with autolamellasomes (LYAL). Black dashed lines indicate clusters of ER fragments.
1175 Boxed regions are magnified on the right. Scale bars, 2 μm for upper images and 1 μm
1176 for upper images.
1177 (L) TEM images from (K) were quantified for the amount of each kind of structure (AL:
1178 autolamellasome, LYAL: lysosome/autolysosome containing with autolamellasome) in
1179 15 μm^2 area. More than 40 cells were imaged for each group. Data are reported as mean
1180 ± SEM.
1181 (M) Quantification of frequency of existence of ER patch per 65 μm^2 area from TEM

images in (K).

(N) Representative TEM images of WT and autophagy-deficient NRK cells expressing doxycycline (Dox)-inducible EGFP-Progerin, induced for 0, 5, or 10 days (D0, D5, D10). Red arrows indicate autolamellasome (LY), and yellow arrow indicates lysosome/autolysosome containing with autolamellasomes (LYAL). Scale bars, 500 nm.

Supplementary videos and information

Supplementary video 1. Continuous formation of ER puncta and their translocation into lysosomes/autolysosomes during Torin1 treatment. Time-lapse live cell imaging of NRK cells stably co-expressing LAMP1-mStaygold and HaloTag-REEP5 treated with 1 μM Torin1**.** Cells were imaged under Olympus FV4000 confocal microscope**.** Scale bar, 10 μm.

Supplementary video 2. Continuous formation of ER puncta and their colocalization with LC3 during Torin1 treatment. Time-lapse live cell imaging of NRK cells stably co-expressing BFP-LC3 and mCherry-REEP5 treated with 1 μM Torin1 starting at 4 h and imaged on an Olympus FV4000 confocal microscope**.** Scale bar, 10 μm.

Supplementary video 3. FRAP analysis of ER patch. *Atg7* KO NRK cells stably expressing mCherry-REEP5 were primed with 200 μM oleic acid for 24 h, then treated with 1 μM Torin1 for 20 h. Cells were photobleached and imaged on a Nikon AX R microscope. Scale bar, 10 μm.

Supplementary video 4. Continuous transition from ER patches to ER puncta during Torin1 treatment. Time-lapse live cell imaging of NRK cells stably co-expressing Lamp1-YFP and mCherry-REEP5. Cells were pretreated with 200 μM oleic

acid for 24 h, then treated with 1 μM Torin1 and imaged on an Olympus FV4000 confocal microscope. Scale bar, 10 μm.

Resource availability

Further information and requests for resources and reagents should be directed to and will be fulfilled by the lead contact, Li Yu. All data supporting the findings of this study are available from the corresponding author upon reasonable request.

Acknowledgements

This research was supported by Tsinghua University Dushi Program (grant no. 20251080019), the Ministry of Science and Technology of the People's Republic of China (grant no. 2024YFA1307301，2024YFF1502900), the National Natural Science Foundation of China (grant no. 32030023，92354306，and 32330025), Tsinghua-Toyota Joint Research Fund (grant no. 20233930058), and Scientific and Technological Innovation Project of China Academy of Chinese Medical Sciences (grant no.CI2023C024YL). We sincerely show our gratefulness to the State Key Laboratory of Membrane Biology for confocal microscopy imaging and facility support. We are grateful to Yan Yang, Chenguang Zhao, Yanfei Hu, Qian Li from the Cell Biology Facility affiliated with the Center of Biomedical Analysis, Tsinghua University, for technical assistance and equipment support. We thank SLSTU-Nikon Biological Imaging Center for microscopy imaging and facility support. We thank Dr. Dachuan Zhang (Tsinghua University, Dr. Li Yu's lab) for providing NRK-*Atf4*-KO, NRK-*Atf6*-KO, NRK-*Xbp1*-KO cells. We thank Dr. Jiayu He (Xinjiang Medical University, Dr. Na Mi's lab) for providing NRK-*Atg14*-KO cells. We thank Dr. Du Feng from Guangzhou Medical University for providing HeLa-*ATG7*-KO cells and its wildtype HeLa cells. We thank Dr. Michael Lazarou from Monash University for providing HeLa-*ATG8*-hexa KO cells and its wildtype HeLa cells. We thank Dr. Xiangyang Wang from Dr. Chuanmao Zhang's lab (Peking University, Kunming University of Science and Technology) for providing human dermal fibroblast (HDF) cells. We thank Dr. Zheng

Jiang from Dr. Anming Meng's lab (Tsinghua University) for providing mouse zygotes. We thank Dr. Wenfeng Fu from Dr. Dong Li's lab (Tsinghua University) for providing the LAMP1-mStaygold and the Calnexin-HaloTag plasmids. We thank Dr. Xiong Ji from Peking University for proving the pMK243 (Tet-OsTIR1-PURO) plasmid.

Author contributions

L.Y. and D.L. conceived and designed the study. L.Y. supervised the project and wrote the manuscript. D.L. performed cell biology, molecular biology, biochemistry and EM experiments. R.Z. performed cryo-EM experiments. W.S., D.Z. and Y.Y. participated in generation of knockout cells. X.S. and H.Z. isolated primary cells from mouse tissues. All authors reviewed and approved the final manuscript.

Declaration of interests

L.Y. is the scientific founder of Migrasome therapeutics Ltd. All other authors declare no conflicts of interest.

Materials and Methods

All research adhered to the guidelines from the Academic Integrity and Ethics committee of Tsinghua University.

Reagents

Torin1 (MCE, HY-13003), ER-Tracker™ Blue-White DPX (ThermoFisher, E12353), 3,3′-Diaminobenzidine tetrahydrochloride hydrate (DAB tetrahydrochloride hydrate, Sigma-Aldrich, D5637), Hydrogen peroxide (Sigma-Aldrich, 88597), Rapamycin (MCE, HY-10219), Sodium oleate (Sigma-Aldrich, O7501), Chloroquine (MCE, HY-17589A); ATP (ThermoFisher, R0441); GTP (Sangon Biotech, A620332-0250); Creatine Phosphate 2Na (Lablead, 0271); Creatine Kinase (Yeasen, 14502ES10); Apotracker Green (BioLegend, 427401); Propidium iodide Staining Solution (Yeasen, 40710ES03); Cy5 (Solarbio, S1053); Lysotracker (Invitrogen, L12492); Magic Red

(Abcam, ab270772)); SirTubulin (Cytoskeleton, Inc., CY-SC002); Doxorubicin hydrochloride (MCE, HY-15142); TBHP (tert-Butyl hydroperoxide solution, Aladdin, B106035), G418 sulfate (Amresco, E859), Hygromycin B (Roche, 10843555001), Puromycin (ThermoFisher, A1113803), Doxycycline (Sigma-Aldrich, D3072), Vigofect (Vigorous, T001), Senescence β-Galactosidase Staining Kit (Beyotime, C0602), Collagenase I (Solarbio, C8140), Collagenase IV (Yeasen, 40510ES76), DNaseI (Aladdin, D106200), Liberase (Sigma-Aldrich, 05401127001).

Antibodies

RTN3 (Proteintech Cat# 12055-2-AP, RRID:AB_2301357); FAM134B (Proteintech Cat# 21537-1-AP, RRID:AB_2878879); TEX264 (Proteintech Cat# 25818-1-AP, RRID:AB_2880272); ATL3 (Proteintech Cat# 16921-1-AP, RRID:AB_2290228); SEC62 (Abcam Cat# ab140644); REEP5 (Proteintech Cat# 14643-1-AP, RRID:AB_2923648); REEP5 (Proteintech Cat# 68119-1-Ig, RRID: AB_2178440); SEC61B (Abcam Cat# ab15576, RRID:AB_301985); Calnexin (Abcam Cat# ab22595, RRID:AB_2069006); p62 (SQSTM1) (MBL International Cat# PM045, RRID:AB_1279301); GAPDH (Proteintech Cat# 60004-1-Ig, RRID:AB_2107436); LAMP1 (Sigma-Aldrich Cat# L1418, RRID:AB_477157); LAMP1 (Enzo Life Sciences Cat# ADI-VAM-EN001, RRID:AB_10630197); mCherry-Tag (Easybio Cat# BE2026, RRID:AB_2936383); ATF4 (Proteintech Cat# 10835-1-AP, RRID:AB_2058600); SEC22B (Synaptic Systems Cat# 186 003, RRID:AB_993020); SAR1B (Proteintech Cat# 15453-1-AP, RRID:AB_2183985); SEC23A (Abcam Cat# ab137582); ATG5 (Cell Signaling Technology Cat# 12994, RRID:AB_2630393); ATG7 (Cell Signaling Technology Cat# 8558, RRID:AB_10831194); ATG9A (Abcam Cat# ab108338, RRID:AB_10863880); ATG14 (Cell Signaling Technology Cat# 96752, RRID:AB_2737056); ATG16L (Cell Signaling Technology Cat# 8089, RRID:AB_10950320); ATG13 (Cell Signaling Technology Cat# 13273, RRID:AB_2798169); Beclin-1 (Cell Signaling Technology Cat# 3495, RRID:AB_1903911); ULK1 (Cell Signaling Technology Cat# 8054,

RRID:AB_11178668); FIP200 (Cell Signaling Technology Cat# 12436, RRID:AB_2797913); WIPI2 (abcepta Cat# AP13314a, RRID:AB_11136530); ATG3 (Cell Signaling Technology Cat# 3415, RRID:AB_2059244); PI4KIIA (Proteintech Cat# 15318-1-AP, RRID:AB_2268225); VPS13C (Proteintech Cat# 28676-1-AP, RRID:AB_2881191); SCAP (Abcam Cat# EPR26242-60); p70(S6K) (Cell Signaling Technology Cat# 2708, RRID:AB_390722); Phospho-p70(S6K) (Thr389) Antibody (Cell Signaling Technology Cat# 9206, RRID:AB_330944); Phospho-p70 (S6K) (Thr389) Antibody (Proteintech Cat# 28735-1-AP, RRID:AB_2918197); Phospho-p70(S6K) (Thr229) Antibody (Proteintech Cat# 81592-1-RR, RRID:AB_2935429); Goat Anti-Rabbit IgG (H+L) (Jackson Cat#111-035-003, RRID:AB_2313567); Goat Anti-Mouse IgG (H+L) (Jackson Cat#115-035-003, RRID:AB_10015289); Goat anti-Rabbit IgG (H+L) Highly Cross-Adsorbed Secondary Antibody, Alexa Fluor 546 (ThermoFisher Cat#A-11035, RRID:AB_2534093); Goat anti-mouse IgG (H+L) Highly Cross-Adsorbed Secondary Antibody, Alexa Fluor 488 (ThermoFisher, Cat#A-11029, RRID:AB_2534093).

Overexpression plasmids and stable cell lines

mCherry-REEP5, HaloTag-REEP5, mCherry-SEC61B, BFP-LC3 were constructed on the PiggyBac transposon vector (RRID:Addgene_210330; RRID:Addgene_210332). LAMP1-YFP was constructed on the pEYFP-N1 vector. ER-DsRed was purchased from Addgene (DsRed2-ER-5, RRID:Addgene_55836). EGFP-REEP5, APEX2-EGFP-REEP5, APEX2-EGFP-SEC61B, EGFP-LC3, were constructed on the pEGFP-C1 vector. APEX2-mCherry-LC3 was constructed on the pmCherry-C1 vector. EGFP-Progerin was constructed on the pMK243 vector (Tet-OsTIR1-PURO) (this plasmid is a kind gift from Dr. Chuanmao Zhang's lab). LAMP1-mStaygold and Calnexin-HaloTag were kind gifts from Dr. Dong Li's lab (Tsinghua University). Stable NRK cell lines expressing the following fluorescent fusion proteins were generated via electroporation, antibiotic selection (hygromycin, G418 sulfate, and puromycin), and FACS sorting: LAMP1-YFP/mCherry-REEP5, APEX2-EGFP-REEP5, APEX2-EGFP-

SEC61B, EGFP-REEP5, LAMP1-YFP/HaloTag-REEP5, LAMP1-mStaygold/Calnexin-HaloTag, LAMP1-YFP/mCherry-SEC61B, LAMP1-YFP/ER-DsRed, BFP-LC3/LAMP1-YFP/mCherry-REEP5, EGFP-LC3/mCherry-REEP5, and APEX2-mCherry-LC3.

Generation of KO cell lines

All the knockout cell lines were generated with CRISPR-Cas9 system. Genes of interest were deleted using a modified PX458 plasmid or PX459 plasmid (provided by Wei Guo from Zhejiang University, Haining, China) that contains two single guide RNAs (sgRNAs) coupled with Cas9 nuclease. The sgRNAs were designed at the website of Broad Institute (https://portals.broadinstitute.org/gppx/crispick/public). Cells transfected with PX458 were seeded into 96-well plates by fluorescence-activated cell sorter selection of EGFP signal expression. Cells transfected with PX459 were selected with puromycin for 7 days and then seeded into 96-well plates by FACS. Genotyping PCR, Western blotting and qPCR were applied for knockout verification.

The targeted genome sequence pairs (two sites slicing) are listed below:

Fam134b-gRNA1: 5’-GCCACTGCATTGCAGAATCA-3’

Fam134b-gRNA2: 5’-CAGAAGAAACGTGAGAGATC-3’

Sec62-gRNA1: 5’-ACAGTTGAATCGAAGATACT-3’

Sec62-gRNA2: 5’-AAATGGGCAAAGGCCAAGAA-3’

Tex264-gRNA1: 5’-GGAGGCTCCTTACCGTCTGG-3’

Tex264-gRNA2: 5’-AGGTGGATGAGCTCAGGTGA-3’

Atl3-gRNA1: 5’-GCTCTGACCCAGAAACTACT-3’

Atl3-gRNA2: 5’-TGAGCTAGAAGAGAGAGCCT-3’

Ccpg1-gRNA1: 5’-CATGCTAATAGCAATCACCA-3’

Ccpg1-gRNA2: 5’-ATTAAAGATGACCTTAACCT-3’

Sar1b-gRNA1: 5’-ATATTTGACTGGATTTACAG-3’

Sar1b -gRNA2: 5’-TCCTTGGATTGGATAATGCC-3’

Sec23a-gRNA1: 5’-AGGACAGGCTCGTACTGAAT-3’

1356 *Sec23a*-gRNA2: 5’-GATATCCCAGCATATGTAGG-3’

1357 *Atg5*-gRNA1: 5’-AAGAGTCAGCTATTTGACGC-3’

1358 *Atg5*-gRNA2: 5’-TCCGTGCAAGGATGCAGTTG-3’

1359 *Atg7*-gRNA1: 5’-GAACGAGTATCGCCTGGACG-3’

1360 *Atg7*-gRNA2: 5’-TGACGCCTTCAGTTCGACAC-3’

1361 *Atg9a*-gRNA1: 5’-AGGCCGAGTACAAACGTGGA-3’

1362 *Atg9a*-gRNA2: 5’-GAGCTGGGCAAACTCGTCCC-3’

1363 *Atg16l1*-gRNA1: 5’-AAAAGCACGACGTACCAAAT-3’

1364 *Atg16l1*-gRNA2: 5’-AGAAGCCAATCGCCTTAATG-3’

1365 *Atg13*-gRNA1: 5’-GTCGAGCCTGGACAATCACT-3’

1366 *Atg13*-gRNA2: 5’-GATCTCACTCAAGACTTCTG-3’

1367 *Beclin1*-gRNA1: 5’-CCTGGACCGAGTGACCATTC-3’

1368 *Beclin1*-gRNA2: 5’-GGAAGAGGCTAACTCAGGAG-3’

1369 *Ulk1*-gRNA1: 5’-ATCATGTCCCAGCACTACGA-3’

1370 *Ulk1*-gRNA2: 5’-GTGGTGGAAAAATTCATCTG-3’

1371 *Wipi2*-gRNA1: 5’-ACTGCTACTTGGCGTACCCA-3’

1372 *Wipi2*-gRNA2: 5’-GCTCTATATACACAACATCC-3’

1373 *Atg3*-gRNA1: 5’-GTAGACACGTACCATAACAC-3’

1374 *Atg3*-gRNA2: 5’-AGGGGAAGAATTGAAAGTGA-3’

1375 *Pi4k2a*-gRNA1: 5’-TTAGGGTTAAGGTTCCCGTA-3’

1376 *Pi4k2a* -gRNA2: 5’-ATTGACCGAGTAAAGTCCAG-3’

1377 *Vps13c*-gRNA1: 5’-TTAGAACACTGGTACGTCAC-3’

1378 *Vps13c*-gRNA2: 5’-TGGTTAGAAATGCACCATAC-3’

1379 *Npc2*-gRNA1: 5’-CAGGAATAGGGAAGTAGACT-3’

1380 *Npc2*-gRNA2: 5’-AAAGGTGACGTTGACACTGT-3’

1381 *Scap*-gRNA1: 5’-TCTGTCCCGAGCATTCCAAC-3’

1382 *Scap*-gRNA2: 5’-ACCTACCCGCCATTGAGTGT-3’

1383 *Srebf1*-gRNA1: 5’-AGGCTTGAGTACCCCAGCAC-3’

1384 *Srebf1*-gRNA2: 5’-AGCATGCCTCGGCTATGTGA-3’

NRK-*Perk*-KO, NRK-*Sec22b*-KO, NRK-*Atg2*-KO, NRK-*p62*-KO, MEF-*Fip200*-KO, HeLa-*ATG8*-hexa KO cells were reported before[46,63-66]. NRK-*Atf4*-KO, NRK-*Atf6*-KO, NRK-*Xbp1*-KO cells were kind gifts from Dr. Dachuan Zhang (Tsinghua University, Li Yu's lab), NRK-*Atg14*-KO cell line was a kind gift from Dr. Jiayu He (Xinjiang Medical University, Dr. Na Mi's lab).

Cell culture

S2 cells were cultured at 28 °C and 5% CO_2 in Schneider's Drosophila medium supplemented with 10% fetal bovine serum, 1% penicillin-streptomycin and 1% Glutamax. MDA-MB-231 cells were cultured at 37 °C and 5% CO_2 in RPMI-1640 high glucose medium supplemented with 10% fetal bovine serum, 1% penicillin-streptomycin and 1% Glutamax. THP1 cells were cultured at 37 °C and 5% CO_2 in RPMI-1640 high glucose medium supplemented with 10% fetal bovine serum, 1% penicillin-streptomycin, 1% Glutamax and 100 ng/mL PMA. The isolated fascia fibroblasts (FFB) and the isolated mouse endometrial stromal cells (MESC) were cultured at 37 °C and 5% CO_2 in DMEM/F-12 medium supplemented with 10% fetal bovine serum, 1% penicillin-streptomycin and 1% Glutamax. The isolated hepatocytes were cultured at 37 °C and 5% CO_2 in Williams E Medium supplemented with 5% fetal bovine serum, 1% penicillin-streptomycin and 1% Glutamax. Other cells were cultured at 37 °C and 5% CO_2 in DMEM high glucose medium supplemented with 10% fetal bovine serum, 1% penicillin-streptomycin and 1% Glutamax.

Immunofluorescence and live cell imaging

For immunofluorescence, cells were grown on confocal dishes and fixed by 4% paraformaldehyde (PFA) at room temperature for 15 min. Then, samples were blocked and permeabilized in PBS containing 0.03% saponin and 10% FBS for 30 minutes at room temperature. Following was incubation with primary antibodies diluted in PBS containing 10% FBS overnight at 4°C. After washing three times with PBS, cells were incubated with secondary antibodies diluted in PBS containing 10% FBS for 1 h at

room temperature in the dark. After final washes with PBS, the samples were imaged with light microscopes.

For live cell imaging, cells were seeded on 3.5mm confocal dishes and monitored with microscopes equipped with a Chamlide environmental incubator system, which maintained the cells at 37 °C and 5% CO_2. Confocal images were acquired with Olympus (FV3000, FV4000) and Nikon (A1HD25, AX R). SIM images were acquired with a Nikon N-SIM microscope equipped with a 100×oil-immersion objective (NA 1.49). Images were reconstructed and analyzed with cellSens software (Olympus), NIS-Elements AR software (Nikon) or ImageJ software (NIH). Z-stack images were reconstructed with Imaris software.

Western blotting and intensities analysis

Cells were solubilized in lysis buffer (2.5% SDS, 50 mM Tris-HCl, pH 7.4) and denatured at 95°C for 15 min. Following protein quantification with the BCA assay kit (Thermo Fisher, 23227), samples were separated on precast SDS-PAGE gradient gels (Lablead; Epizyme) and electroblotted onto PVDF membranes (Millipore, ISEQ00010). The membranes were blocked in TBST (20 mM Tris-HCl, pH 7.6, 137 mM NaCl and 0.2% Tween-20) containing 5% milk for 1 h at room temperature. Primary antibodies were diluted in Solution I (TOYOBO, NKB-201). After incubation with primary antibodies at 4 °C overnight, the membranes were washed with TBST and then incubated with horseradish peroxidase (HRP)-conjugated secondary antibodies diluted in antibody solution buffer (NCM Biotech, WB100D) at room temperature for 1 h. After final washes with TBST, the membranes were detected and quantified with ChemiDoc Touch Imaging System (Bio-Rad, ChemiDoc MP, RRID:SCR_021693) using Westar ETAC (Cyanagen).

Band intensities were quantified using either ImageLab software (Bio-Rad) or ImageJ software (NIH). For ImageLab software (Bio-Rad), lanes were automatically detected and manually adjusted for alignment. Background subtraction was applied using the rolling disk method. Band volumes (integrated intensity) were measured and

normalized to the corresponding loading control (e.g., Actin or GAPDH) from the same lane. For ImageJ software (NIH), images were converted to 8-bit grayscale format, and background subtraction was performed using the "Rolling ball radius" method. Proteins of interest were selected using rectangular selections, and lane boundaries were manually defined. The integrated density values were measured and normalized to the corresponding loading control from the same blot. Data from at least three independent biological replicates were analyzed and expressed as fold change relative to the control group.

Quantitative real-time PCR

Total RNA was extracted with MolPure® Flash Cell/Tissue Total RNA Kit (Yeasen, 19221ES50). cDNA was synthesized using a ReverTra Ace qPCR RT Kit (TOYOBO, FSQ-101). Quantitative real-time PCR was performed using 2× T5 Fast qPCR Mix (SYBR Green I) (TSINGKE Biological Technology, TSE202). Primer sequences are provided below:

Ccpg1-1F: 5’-GTCACTGGCGTCTGGAGC-3’

Ccpg1-1R: 5’-TCAGACATTTTTCAGGTCCGAAG-3’

Ccpg1-2F: 5’-CGCGAGCAGGTTGTTGTT-3’

Ccpg1-2R: 5’-TTCAGACATTTTTCAGGTCCGA-3’

Npc2-F: 5’-CCTGAGCCTGACGGTTGTAA-3’

Npc2-R: 5’-CACCACCAGTTTTAGAGAGGG-3’

Srebf1-F: 5’-CTTGACCGACATCGAAGACAT-3’

Srebf1-R: 5’-CCAGCATAGGGGGCATCAAA-3’

Label-free Mass Spectrum

For protein extraction, cells were lysed in 10 volumes of ice-cold lysis buffer (1% sodium deoxycholate, 10 mM Tris-HCl, pH 8.5), immediately boiled at 100 °C for 10 min to inactivate proteases, and sonicated on a pre-chilled (4 °C) non-contact ultrasonicator (30 s on/30 s off, 15 cycles). Lysates were cleared by brief centrifugation,

and supernatants were stored at -80 °C until analysis. Protein concentration was determined by BCA assay. Label-free quantitative proteomic analysis was performed by Protein Chemistry and Proteomics Platform (Technology Center for Protein Sciences, Tsinghua University) using three biological replicates.

TEM

Cells were cultured on 3.5 mm confocal dishes and fixed in 2.5% glutaraldehyde (GA) (Legene). The cells were washed with 0.1 M PB buffer (pH 7.2) three times, and post-fixed in 1% osmium tetroxide (Ted Pella)/1.5% K3[Fe(CN)6] in distilled water for 30 min at 4 °C. After three washes with distilled water, the samples were stained with 1% uranyl acetate overnight at 4°C in the dark. After three washes with distilled water, the cells were dehydrated in a graded ethanol series (50%, 70%, 80%, 90%, 100%, 100%, 100%, for 2 min each on ice, then 100%, 5 min at RT). The cells were infiltrated in Pon 812 (SPI) resin (50%, 67%, 75% for 30 min each, then 100% for 1 h and 100% overnight at RT), and then polymerized at 60 °C for 48 h. Ultrathin sections of 70 nm were cut by ultramicrotome (Leica EM UC7). After staining with uranyl acetate and lead citrate, sections were observed under 120 kV transmission electron microscope (Hitachi, HT-7800).

CLEM

Cells grown on gridded glass-bottom dishes (Cellvis, D35-14-1.5GI) were fixed with 4% PFA and immediately imaged with confocal microscope to document the cells of interest at different magnifications. After that, the cells were post-fixed with 2.5% GA and prepared for TEM. The steps for preparing ultrathin sections were the same as standard TEM sample preparation protocols.

APEX2-TEM

Cells stably expressing APEX2-EGFP-REEP5 (or APEX2-EGFP-SEC61B, APEX2-mCherry-LC3) were cultured on 3.5 mm confocal dishes and fixed with 2.5% GA. All

subsequent steps were performed on ice within 1 h of fixation. After three washes with 0.1M PB buffer (PH 7.2), cells were incubated in a freshly prepared solution of 0.5 mg/mL (1.4 mM) DAB tetrahydrochloride (Sigma, D5637) in 0.1M PB buffer (PH 7.2) for 20 min. Next, a fresh solution containing 0.5 mg/mL (1.4 mM) DAB and 0.03% (v/v) H_2O_2 was used for the enzymatic reaction. After reaction, the cells were washed three times with 0.1M PB buffer (PH 7.2). Post-fixation staining was performed with 2% osmium tetroxide for 5 min. Cells were then rinsed three times in distilled water, and placed in 2% aqueous uranyl acetate (Electron Microscopy Sciences) overnight. Subsequent steps followed standard TEM sample preparation protocols.

FIB-SEM

The resin block was trimmed to expose cells at the surface, then coated with a ~20-nm gold layer followed by a ~600-nm platinum layer applied perpendicular to the block face. Imaging was performed on a Helios NanoLab G3 UC scanning electron microscope in back-scattered electron (BSE) mode using TLD (through-the-lens) and ICD (in-column) detectors. Each milling cycle used a 30 kV, 0.79 nA ion beam to remove a 10-nm-thick surface layer, and images were acquired with a 2 kV, 0.4 nA electron beam at 8 μs/pixel dwell time.

Sample Vitrification

For sample preparation, a cell suspension with a concentration of approximately 3×10^6 cells/mL was used. 200-mesh copper grids with a continuous carbon film (EMCN, BZ1011125a) were rendered hydrophilic by glow-discharging in ambient air for 25 seconds at 15 mA using a Pelco EasiGlow glow-discharge system. The vitrification process was carried out using a Leica EM GP2 automatic plunge-freezer, operated within an environmental chamber maintained at 25°C and 75% relative humidity to minimize sample evaporation.

A volume of 3 μL of the suspended cell solution was applied to the carbon-coated side of the glow-discharged grid. To achieve a thin, uniform layer of cells suitable for

imaging, 2 μL of buffer was applied to the reverse side of the grid. The grid was blotted from the reverse side for 4-6 s and immediately plunged into liquid ethane cooled by liquid nitrogen, resulting in the vitrification of the sample. Grids were subsequently stored in liquid nitrogen until required for further processing.

Cryo-lamella preparation

Lamellae were prepared from the vitrified cells using a multi-step milling procedure analogous to established protocols[67] with a Helios dual-beam cryo-focused ion beam/scanning electron microscope (cryo-FIB/SEM) (Thermo Fisher Scientific). To balance milling speed with precision and minimize beam-induced sample damage during the milling process, the Ga^{2+} ion beam current at an accelerating voltage of 30 kV was progressively reduced from 0.79 nA for rough milling to 24 pA for final polishing. This procedure yielded lamellae with a final thickness between 100 to 200 nm.

Cryo-electron tomography data collection

Lamellae were imaged on a 300 kV Titan Krios electron microscope (Thermo Fisher Scientific) equipped with a Gatan post-column energy filter. Images were recorded at a magnification of ×53,000, resulting in a calibrated pixel size of 2.4 Å. Tilt-series were collected using the bidirectional tilt scheme over a range of ±60°, with a 2° angular increment. A target defocus of approximately -5 μm was applied, and the total cumulative electron dose for each tilt-series was limited to 120 $e^{-}/Å^{2}$.

Tomogram reconstruction

Following data acquisition, the raw movie frames were processed to correct for specimen drift and beam-induced motion using MotionCor2[68]. The resulting tilt-series were subsequently aligned using patch tracking routine and reconstructed into tomograms by weighted back-projection, employing the IMOD software suite[69]. To enhance the signal-to-noise ratio for visualization and subsequent segmentation, the

final tomograms were four-fold binned, and a SIRT-like filter was applied.

Tomogram segmentation and visualization

Three-dimensional segmentation of cellular features within the reconstructed tomograms was performed using Amira (Thermo Fisher Scientific). A semi-automated workflow was employed to generate accurate 3D models of membranes and other structures of interest, which combined automated feature recognition with subsequent manual refinement. Features such as membranes were first identified using threshold-based tools within the software. Each segmented feature was then manually inspected, corrected, and annotated, to ensure anatomical accuracy and remove any artifacts from the automated process. The finalized 3D models were then rendered within Amira for visualization and analysis.

FRAP

Fluorescence recovery after photobleaching (FRAP) experiments were performed using a Nikon AX R confocal microscope equipped with a 100×oil-immersion objective. After acquiring five prebleach frames (1s intervals), a circular region of interest (ROI; 1 μm diameter) was photobleached with the 488 nm laser at 100% power for 5 s. Postbleach recovery was recorded at 1-s intervals for 60 s. Mean fluorescence intensity within the bleached ROI was quantified at each time point, background-subtracted using an extracellular ROI, corrected for acquisition photobleaching by normalization to an unbleached reference ROI in the same cell, and expressed relative to the mean prebleach intensity (set as 100%). Recovery curves were plotted as mean ± SEM from >20 cells per condition using GraphPad Prism 10 software.

Isolation of primary cells

In this project, we isolated several primary cells from mouse tissues, including lung fibroblasts (LFB), fascia fibroblasts (FFB), dermal fibroblasts (DFB), hepatocytes, mouse embryonic fibroblasts (MEF) and mouse endometrial stromal cells (MESC),

following previously described protocols[70-74].

Human dermal fibroblasts (HDF) from healthy donors and HGPS patients were obtained from Dr. Chuanmao Zhang's lab, as previously reported[61].

In vitro reconstitution

S150 cell extract preparation: Cells were harvested and washed with cold PBS, and resuspended in 2× cytosol buffer (50 mM Hepes-KOH, 50 mM KOAc, 2.5 mM MgCl2, 250 mM sucrose, PH 7.4) containing protease inhibitors. Lysis was performed by mechanical disruption (25G needle or homogenizer) until >80% efficiency was confirmed by typan blue (Solarbio Life Sciences, C0040) staining. The lysate was centrifuged sequentially at 1,000×g for 10 min and 120,000×g for 20 min at 4°C. The supernatant was then ultracentrifuged at 150,000×g for 1 h at 4°C. The final S150 supernatant was acquired, protein concentration was determined by BCA assay (~10 mg/mL), and aliquots were flash-frozen in liquid nitrogen and stored at -80°C.

We have tried several protocols for *in vitro* reconstitution, the most efficient is described below. After incubation with 200 μM oleic acid for 20 h, cells grown on 3.5 mm confocal dishes were treated with reaction buffer (25 mM Hepes-KOH, 25 mM KOAc, 1.25 mM MgCl2, 125 mM sucrose, PH 7.4) containing 40 μg/mL digitonin and protease inhibitors alone (mock group), or additionally supplemented with 50% S150 and an energy system (1 mM ATP, 0.5 mM GTP, 20 mM creatine phosphate, 0.2 mg/mL creatine kinase) (all group). Both groups were incubated at 30°C for 6-8 h to allow reconstitution, then fixed with 2.5% GA for TEM analysis. Cell death was confirmed using Apotracker and PI, and plasma membrane permeabilization was assessed with Cy5.

Negative staining TEM

A droplet of S150 or resuspended P150 was deposited onto copper grids for 5 minutes. Excess sample was blotted with filter paper. The grid was promptly washed with a droplet of double distilled water (ddH_2O), stained with 1% uranyl acid for one minute,

1617 and washed twice with droplets of ddH_2O. Residual water was blotted using filter paper,
1618 and the grid was air-dried before imaging by transmission electron microscopy (TEM).
1619

1620 **Statistical analysis**

1621 Normality was assessed using a Kolmogorov-Smirnov test. Statistical analyses were
1622 conducted with GraphPad Prism 10 using an unpaired two-tailed Student's t-test.
1623 Sample sizes were determined empirically without a priori statistical calculations, and
1624 all acquired data were retained for analysis. Error bars indicate mean ± SEM. *P<0.05,
1625 **P<0.01, ***P<0.001, ****P<0.0001, ns, not significant.
1626
1627

1628 **References**

1629 1. Tsukada, M., and Ohsumi, Y. (1993). Isolation and characterization of autophagy-defective
1630 mutants of Saccharomyces cerevisiae. FEBS Lett *333*, 169-174. 10.1016/0014-
1631 5793(93)80398-e.
1632 2. Takeshige, K., Baba, M., Tsuboi, S., Noda, T., and Ohsumi, Y. (1992). Autophagy in yeast
1633 demonstrated with proteinase-deficient mutants and conditions for its induction. J Cell
1634 Biol *119*, 301-311. 10.1083/jcb.119.2.301.
1635 3. Mizushima, N., Noda, T., Yoshimori, T., Tanaka, Y., Ishii, T., George, M.D., Klionsky, D.J.,
1636 Ohsumi, M., and Ohsumi, Y. (1998). A protein conjugation system essential for autophagy.
1637 Nature *395*, 395-398. 10.1038/26506.
1638 4. Kametaka, S., Matsuura, A., Wada, Y., and Ohsumi, Y. (1996). Structural and functional
1639 analyses of APG5, a gene involved in autophagy in yeast. Gene *178*, 139-143.
1640 10.1016/0378-1119(96)00354-x.
1641 5. Deretic, V., Saitoh, T., and Akira, S. (2013). Autophagy in infection, inflammation and
1642 immunity. Nat Rev Immunol *13*, 722-737. 10.1038/nri3532.
1643 6. Mizushima, N., and Komatsu, M. (2011). Autophagy: renovation of cells and tissues. Cell
1644 *147*, 728-741. 10.1016/j.cell.2011.10.026.
1645 7. Deretic, V., and Klionsky, D.J. (2008). How cells clean house. Sci Am *298*, 74-81.
1646 10.1038/scientificamerican0508-74.
1647 8. Klionsky, D.J., and Emr, S.D. (2000). Autophagy as a regulated pathway of cellular
1648 degradation. Science *290*, 1717-1721. 10.1126/science.290.5497.1717.
1649 9. Gómez-Sánchez, R., Tooze, S.A., and Reggiori, F. (2021). Membrane supply and
1650 remodeling during autophagosome biogenesis. Curr Opin Cell Biol *71*, 112-119.
1651 10.1016/j.ceb.2021.02.001.
1652 10. Nishimura, T., and Tooze, S.A. (2020). Emerging roles of ATG proteins and membrane
1653 lipids in autophagosome formation. Cell Discov *6*, 32. 10.1038/s41421-020-0161-3.
1654 11. Kirkin, V., McEwan, D.G., Novak, I., and Dikic, I. (2009). A role for ubiquitin in selective

1655 autophagy. Mol Cell *34*, 259-269. 10.1016/j.molcel.2009.04.026.
1656 12. Vargas, J.N.S., Hamasaki, M., Kawabata, T., Youle, R.J., and Yoshimori, T. (2023). The
1657 mechanisms and roles of selective autophagy in mammals. Nat Rev Mol Cell Biol *24*, 167-
1658 185. 10.1038/s41580-022-00542-2.
1659 13. Youle, R.J., and Narendra, D.P. (2011). Mechanisms of mitophagy. Nat Rev Mol Cell Biol
1660 *12*, 9-14. 10.1038/nrm3028.
1661 14. Hong, Z., Pedersen, N.M., Wang, L., Torgersen, M.L., Stenmark, H., and Raiborg, C. (2017).
1662 PtdIns3P controls mTORC1 signaling through lysosomal positioning. J Cell Biol *216*, 4217-
1663 4233. 10.1083/jcb.201611073.
1664 15. Li, W., He, P., Huang, Y., Li, Y.F., Lu, J., Li, M., Kurihara, H., Luo, Z., Meng, T., Onishi, M., et
1665 al. (2021). Selective autophagy of intracellular organelles: recent research advances.
1666 Theranostics *11*, 222-256. 10.7150/thno.49860.
1667 16. Pankiv, S., Clausen, T.H., Lamark, T., Brech, A., Bruun, J.A., Outzen, H., Øvervatn, A., Bjørkøy,
1668 G., and Johansen, T. (2007). p62/SQSTM1 binds directly to Atg8/LC3 to facilitate
1669 degradation of ubiquitinated protein aggregates by autophagy. J Biol Chem *282*, 24131-
1670 24145. 10.1074/jbc.M702824200.
1671 17. Birgisdottir Å, B., Lamark, T., and Johansen, T. (2013). The LIR motif - crucial for selective
1672 autophagy. J Cell Sci *126*, 3237-3247. 10.1242/jcs.126128.
1673 18. Noda, N.N., Ohsumi, Y., and Inagaki, F. (2010). Atg8-family interacting motif crucial for
1674 selective autophagy. FEBS Lett *584*, 1379-1385. 10.1016/j.febslet.2010.01.018.
1675 19. Lamark, T., and Johansen, T. (2021). Mechanisms of Selective Autophagy. Annu Rev Cell
1676 Dev Biol *37*, 143-169. 10.1146/annurev-cellbio-120219-035530.
1677 20. Grumati, P., Dikic, I., and Stolz, A. (2018). ER-phagy at a glance. J Cell Sci *131*.
1678 10.1242/jcs.217364.
1679 21. Bravo, R., Parra, V., Gatica, D., Rodriguez, A.E., Torrealba, N., Paredes, F., Wang, Z.V.,
1680 Zorzano, A., Hill, J.A., Jaimovich, E., et al. (2013). Endoplasmic reticulum and the unfolded
1681 protein response: dynamics and metabolic integration. Int Rev Cell Mol Biol *301*, 215-290.
1682 10.1016/b978-0-12-407704-1.00005-1.
1683 22. Schwarz, D.S., and Blower, M.D. (2016). The endoplasmic reticulum: structure, function
1684 and response to cellular signaling. Cell Mol Life Sci *73*, 79-94. 10.1007/s00018-015-2052-
1685 6.
1686 23. Stolz, A., and Grumati, P. (2019). The various shades of ER-phagy. Febs j *286*, 4642-4649.
1687 10.1111/febs.15031.
1688 24. Schuck, S., Gallagher, C.M., and Walter, P. (2014). ER-phagy mediates selective
1689 degradation of endoplasmic reticulum independently of the core autophagy machinery.
1690 J Cell Sci *127*, 4078-4088. 10.1242/jcs.154716.
1691 25. Fregno, I., and Molinari, M. (2019). Proteasomal and lysosomal clearance of faulty
1692 secretory proteins: ER-associated degradation (ERAD) and ER-to-lysosome-associated
1693 degradation (ERLAD) pathways. Crit Rev Biochem Mol Biol *54*, 153-163.
1694 10.1080/10409238.2019.1610351.
1695 26. Chino, H., and Mizushima, N. (2020). ER-Phagy: Quality Control and Turnover of
1696 Endoplasmic Reticulum. Trends Cell Biol *30*, 384-398. 10.1016/j.tcb.2020.02.001.
1697 27. Chino, H., and Mizushima, N. (2023). ER-Phagy: Quality and Quantity Control of the
1698 Endoplasmic Reticulum by Autophagy. Cold Spring Harb Perspect Biol *15*.

1699 10.1101/cshperspect.a041256.
1700 28. Khaminets, A., Heinrich, T., Mari, M., Grumati, P., Huebner, A.K., Akutsu, M., Liebmann, L.,
1701 Stolz, A., Nietzsche, S., Koch, N., et al. (2015). Regulation of endoplasmic reticulum
1702 turnover by selective autophagy. Nature *522*, 354-358. 10.1038/nature14498.
1703 29. Grumati, P., Morozzi, G., Hölper, S., Mari, M., Harwardt, M.I.E., Yan, R., Müller, S., Reggiori,
1704 F., Heilemann, M., and Dikic, I. (2017). Full length RTN3 regulates turnover of tubular
1705 endoplasmic reticulum via selective autophagy. Elife *6*. 10.7554/eLife.25555.
1706 30. Rudinskiy, M., Galli, C., Raimondi, A., and Molinari, M. (2025). The intrinsically disordered
1707 regions of organellophagy receptors are interchangeable and control organelle
1708 fragmentation, ER-phagy and mitophagy flux. Nat Cell Biol *27*, 1431-1447.
1709 10.1038/s41556-025-01728-4.
1710 31. Mo, J., Chen, J., and Zhang, B. (2020). Critical roles of FAM134B in ER-phagy and diseases.
1711 Cell Death Dis *11*, 983. 10.1038/s41419-020-03195-1.
1712 32. Chino, H., Hatta, T., Natsume, T., and Mizushima, N. (2019). Intrinsically Disordered Protein
1713 TEX264 Mediates ER-phagy. Mol Cell *74*, 909-921.e906. 10.1016/j.molcel.2019.03.033.
1714 33. Chen, Q., Xiao, Y., Chai, P., Zheng, P., Teng, J., and Chen, J. (2019). ATL3 Is a Tubular ER-
1715 Phagy Receptor for GABARAP-Mediated Selective Autophagy. Curr Biol *29*, 846-855.e846.
1716 10.1016/j.cub.2019.01.041.
1717 34. Mochida, K., and Nakatogawa, H. (2022). ER-phagy: selective autophagy of the
1718 endoplasmic reticulum. EMBO Rep *23*, e55192. 10.15252/embr.202255192.
1719 35. Smith, M.D., Harley, M.E., Kemp, A.J., Wills, J., Lee, M., Arends, M., von Kriegsheim, A.,
1720 Behrends, C., and Wilkinson, S. (2018). CCPG1 Is a Non-canonical Autophagy Cargo
1721 Receptor Essential for ER-Phagy and Pancreatic ER Proteostasis. Dev Cell *44*, 217-
1722 232.e211. 10.1016/j.devcel.2017.11.024.
1723 36. Pollard, T.D., Earnshaw, W. C., Lippincott-Schwartz, J., and Johnson, G. T. . (2016). Cell
1724 Biology: Third Edition. (Elsevier).
1725 37. Klumperman, J., and Raposo, G. (2014). The complex ultrastructure of the endolysosomal
1726 system. Cold Spring Harb Perspect Biol *6*, a016857. 10.1101/cshperspect.a016857.
1727 38. Germain, D.P. (2010). Fabry disease. Orphanet J Rare Dis *5*, 30. 10.1186/1750-1172-5-30.
1728 39. Wu, S.Z., Liang, X., Geng, J., Zhang, M.B., Xie, N., and Su, X.Y. (2019). Hydroxychloroquine-
1729 induced renal phospholipidosis resembling Fabry disease in undifferentiated connective
1730 tissue disease: A case report. World J Clin Cases *7*, 4377-4383. 10.12998/wjcc.v7.i24.4377.
1731 40. Raposo, G., Marks, M.S., and Cutler, D.F. (2007). Lysosome-related organelles: driving
1732 post-Golgi compartments into specialisation. Curr Opin Cell Biol *19*, 394-401.
1733 10.1016/j.ceb.2007.05.001.
1734 41. Faigle, W., Raposo, G., Tenza, D., Pinet, V., Vogt, A.B., Kropshofer, H., Fischer, A., de Saint-
1735 Basile, G., and Amigorena, S. (1998). Deficient peptide loading and MHC class II
1736 endosomal sorting in a human genetic immunodeficiency disease: the Chediak-Higashi
1737 syndrome. J Cell Biol *141*, 1121-1134. 10.1083/jcb.141.5.1121.
1738 42. Platt, F.M., Boland, B., and van der Spoel, A.C. (2012). The cell biology of disease: lysosomal
1739 storage disorders: the cellular impact of lysosomal dysfunction. J Cell Biol *199*, 723-734.
1740 10.1083/jcb.201208152.
1741 43. Rozenszajn, L.A., Epstein, Y., and Fischer, D. (1969). Myelin figures in blood cells, lysosomes,
1742 and lipidoses. Am J Clin Pathol *52*, 473-476. 10.1093/ajcp/52.4.473.

44. Hurley, J.H., Coyne, A.N., Miączyńska, M., and Stenmark, H. (2025). The expanding repertoire of ESCRT functions in cell biology and disease. Nature *642*, 877-888. 10.1038/s41586-025-08950-y.
45. Schäfer, J.A., Schessner, J.P., Bircham, P.W., Tsuji, T., Funaya, C., Pajonk, O., Schaeff, K., Ruffini, G., Papagiannidis, D., Knop, M., et al. (2020). ESCRT machinery mediates selective microautophagy of endoplasmic reticulum in yeast. Embo j *39*, e102586. 10.15252/embj.2019102586.
46. Xu, F., Du, W., Zou, Q., Wang, Y., Zhang, X., Xing, X., Li, Y., Zhang, D., Wang, H., Zhang, W., et al. (2021). COPII mitigates ER stress by promoting formation of ER whorls. Cell Res *31*, 141-156. 10.1038/s41422-020-00416-2.
47. Mizushima, N., Levine, B., Cuervo, A.M., and Klionsky, D.J. (2008). Autophagy fights disease through cellular self-digestion. Nature *451*, 1069-1075. 10.1038/nature06639.
48. Lam, S.S., Martell, J.D., Kamer, K.J., Deerinck, T.J., Ellisman, M.H., Mootha, V.K., and Ting, A.Y. (2015). Directed evolution of APEX2 for electron microscopy and proximity labeling. Nat Methods *12*, 51-54. 10.1038/nmeth.3179.
49. Fumagalli, F., Noack, J., Bergmann, T.J., Cebollero, E., Pisoni, G.B., Fasana, E., Fregno, I., Galli, C., Loi, M., Soldà, T., et al. (2016). Translocon component Sec62 acts in endoplasmic reticulum turnover during stress recovery. Nat Cell Biol *18*, 1173-1184. 10.1038/ncb3423.
50. An, H., Ordureau, A., Paulo, J.A., Shoemaker, C.J., Denic, V., and Harper, J.W. (2019). TEX264 Is an Endoplasmic Reticulum-Resident ATG8-Interacting Protein Critical for ER Remodeling during Nutrient Stress. Mol Cell *74*, 891-908.e810. 10.1016/j.molcel.2019.03.034.
51. Orsi, A., Razi, M., Dooley, H.C., Robinson, D., Weston, A.E., Collinson, L.M., and Tooze, S.A. (2012). Dynamic and transient interactions of Atg9 with autophagosomes, but not membrane integration, are required for autophagy. Mol Biol Cell *23*, 1860-1873. 10.1091/mbc.E11-09-0746.
52. Judith, D., and Tooze, S.A. (2019). ATG9A supplies PtdIns4P to the autophagosome initiation site. Autophagy *15*, 1660-1661. 10.1080/15548627.2019.1632124.
53. Suzuki, E., Matsuda, T., Kawamoto, T., Takahashi, H., Mieda, Y., Matsuura, Y., Takai, T., Kanno, A., Koyanagi-Kimura, M., Asahara, S.I., et al. (2018). Docosahexaenoic Acid Reduces Palmitic Acid-Induced Endoplasmic Reticulum Stress in Pancreatic B Cells. Kobe J Med Sci *64*, E43-e55.
54. Schuck, S., Prinz, W.A., Thorn, K.S., Voss, C., and Walter, P. (2009). Membrane expansion alleviates endoplasmic reticulum stress independently of the unfolded protein response. J Cell Biol *187*, 525-536. 10.1083/jcb.200907074.
55. Fedele, A.O., and Proud, C.G. (2020). Chloroquine and bafilomycin A mimic lysosomal storage disorders and impair mTORC1 signalling. Biosci Rep *40*. 10.1042/bsr20200905.
56. Ruohola, H., Kabcenell, A.K., and Ferro-Novick, S. (1989). Reconstitution of transport from the ER to the Golgi complex in yeast using microsomes and permeabilized yeast cells. Methods Cell Biol *31*, 143-154. 10.1016/s0091-679x(08)61606-4.
57. Baker, D., Hicke, L., Rexach, M., Schleyer, M., and Schekman, R. (1988). Reconstitution of SEC gene product-dependent intercompartmental protein transport. Cell *54*, 335-344. 10.1016/0092-8674(88)90196-1.
58. López-Otín, C., Blasco, M.A., Partridge, L., Serrano, M., and Kroemer, G. (2023). Hallmarks

of aging: An expanding universe. Cell *186*, 243-278. 10.1016/j.cell.2022.11.001.

59. Chang, B.D., Xuan, Y., Broude, E.V., Zhu, H., Schott, B., Fang, J., and Roninson, I.B. (1999). Role of p53 and p21waf1/cip1 in senescence-like terminal proliferation arrest induced in human tumor cells by chemotherapeutic drugs. Oncogene *18*, 4808-4818. 10.1038/sj.onc.1203078.

60. Chen, Q., and Ames, B.N. (1994). Senescence-like growth arrest induced by hydrogen peroxide in human diploid fibroblast F65 cells. Proc Natl Acad Sci U S A *91*, 4130-4134. 10.1073/pnas.91.10.4130.

61. Wang, X., Ma, L., Lu, D., Zhao, G., Ren, H., Lin, Q., Jia, M., Huang, F., Wang, S., Xu, Z., et al. (2024). Nuclear envelope budding inhibition slows down progerin-induced aging process. Proc Natl Acad Sci U S A *121*, e2321378121. 10.1073/pnas.2321378121.

62. Eriksson, M., Brown, W.T., Gordon, L.B., Glynn, M.W., Singer, J., Scott, L., Erdos, M.R., Robbins, C.M., Moses, T.Y., Berglund, P., et al. (2003). Recurrent de novo point mutations in lamin A cause Hutchinson-Gilford progeria syndrome. Nature *423*, 293-298. 10.1038/nature01629.

63. Sun, D., Wu, R., Zheng, J., Li, P., and Yu, L. (2018). Polyubiquitin chain-induced p62 phase separation drives autophagic cargo segregation. Cell Res *28*, 405-415. 10.1038/s41422-018-0017-7.

64. Sho, T., Li, Y., Jiao, H., and Yu, L. (2024). Migratory autolysosome disposal mitigates lysosome damage. J Cell Biol *223*. 10.1083/jcb.202403195.

65. Nguyen, T.N., Padman, B.S., Usher, J., Oorschot, V., Ramm, G., and Lazarou, M. (2016). Atg8 family LC3/GABARAP proteins are crucial for autophagosome-lysosome fusion but not autophagosome formation during PINK1/Parkin mitophagy and starvation. J Cell Biol *215*, 857-874. 10.1083/jcb.201607039.

66. Ren, J., Liang, R., Wang, W., Zhang, D., Yu, L., and Feng, W. (2020). Multi-site-mediated entwining of the linear WIR-motif around WIPI β-propellers for autophagy. Nat Commun *11*, 2702. 10.1038/s41467-020-16523-y.

67. Wagner, F.R., Watanabe, R., Schampers, R., Singh, D., Persoon, H., Schaffer, M., Fruhstorfer, P., Plitzko, J., and Villa, E. (2020). Preparing samples from whole cells using focused-ion-beam milling for cryo-electron tomography. Nat Protoc *15*, 2041-2070. 10.1038/s41596-020-0320-x.

68. Zheng, S.Q., Palovcak, E., Armache, J.P., Verba, K.A., Cheng, Y., and Agard, D.A. (2017). MotionCor2: anisotropic correction of beam-induced motion for improved cryo-electron microscopy. Nat Methods *14*, 331-332. 10.1038/nmeth.4193.

69. Mastronarde, D.N., and Held, S.R. (2017). Automated tilt series alignment and tomographic reconstruction in IMOD. J Struct Biol *197*, 102-113. 10.1016/j.jsb.2016.07.011.

70. Edelman, B.L., and Redente, E.F. (2018). Isolation and Characterization of Mouse Fibroblasts. Methods Mol Biol *1809*, 59-67. 10.1007/978-1-4939-8570-8_5.

71. Correa-Gallegos, D., Ye, H., Dasgupta, B., Sardogan, A., Kadri, S., Kandi, R., Dai, R., Lin, Y., Kopplin, R., Shenai, D.S., et al. (2023). CD201(+) fascia progenitors choreograph injury repair. Nature *623*, 792-802. 10.1038/s41586-023-06725-x.

72. Xu, Z., Chen, D., Hu, Y., Jiang, K., Huang, H., Du, Y., Wu, W., Wang, J., Sui, J., Wang, W., et al. (2022). Anatomically distinct fibroblast subsets determine skin autoimmune patterns.

Nature *601*, 118-124. 10.1038/s41586-021-04221-8.

73. Charni-Natan, M., and Goldstein, I. (2020). Protocol for Primary Mouse Hepatocyte Isolation. STAR Protoc *1*, 100086. 10.1016/j.xpro.2020.100086.

74. Rizo, J.A., Spencer, T.E., and Kelleher, A.M. (2024). Protocol for the establishment and characterization of an endometrial-derived epithelial organoid and stromal cell co-culture system. STAR Protoc *5*, 102894. 10.1016/j.xpro.2024.102894.